

Modelling coupled subduction and earthquake dynamics

I. van Zelst¹, S. Wollherr², A.-A. Gabriel², E. H. Madden², Y. van Dinther^{1,3}

¹Seismology and Wave Physics, Institute of Geophysics, Department of Earth Sciences, ETH Zürich, Zürich, Switzerland

²Geophysics, Department of Earth and Environmental Sciences, LMU Munich, Munich, Germany

³Department of Earth Sciences, Utrecht University, Utrecht, The Netherlands

Key Points:

- We couple a geodynamic seismic cycle model to a dynamic rupture model to resolve subduction and earthquake dynamics across timescales
- Both events are comparable in terms of nucleation and material-dependent stress drop, but not slip
- Complex lithology leads to various rupture styles and speeds, shallow slip accumulation, and fault reactivation

Corresponding author: Iris van Zelst, iris.vanzelst@erdw.ethz.ch

Abstract

15
16 Studying seismicity requires numerical methods that span a large range of spatial
17 and temporal scales. We present the first coupled framework that resolves subduction
18 dynamics over millions of years and earthquake dynamics down to fractions of a second.
19 Using a two-dimensional geodynamic seismic cycle (SC) method, we model 4 million years
20 of subduction followed by cycles of spontaneous megathrust events. At the initiation of
21 one such SC event, we export the self-consistent fault and surface geometry, fault stress
22 and strength, and heterogeneous material properties to a dynamic rupture (DR) model.
23 Coupling leads to spontaneous dynamic rupture nucleation, propagation and arrest with
24 the same spatial characteristics as in the SC model. It also results in a similar material-
25 dependent stress drop, although dynamic slip is significantly larger. The DR event shows
26 a high degree of complexity, featuring various rupture styles and speeds, precursory phases,
27 and fault reactivation. Compared to a homogeneous coupled model, accounting for re-
28 alistic lithological contrasts doubles the amount of maximum slip, introduces local pulse-
29 like rupture episodes, and relocates the peak slip from near the downdip limit of the seis-
30 mogenic zone to the updip limit. When an SC splay fault is included in the DR model,
31 the rupture prefers the splay over the shallow megathrust, although wave reflections do
32 activate the megathrust afterwards. We conclude that taking the full complexity of sub-
33 duction zones into account is important for realistic modelling and hazard assessment
34 of subduction zone seismicity and associated tsunamis.

1 Introduction

35
36 Throughout the past decades, enigmatic observations of subduction zone earthquakes
37 have repeatedly given rise to speculation. For example, large slip occurring up to the trench
38 during the 2011 M_w 9.0 Tōhoku-Oki earthquake demonstrated how poorly the occurrence
39 of slip in shallow, presumably velocity-strengthening regions is understood to date (Fujiwara
40 et al., 2011; Lay et al., 2011).

41 Understanding the seismic characteristics along megathrusts from the trench to the
42 down-dip limit of the seismogenic zone is crucial for improving the assessment of seis-
43 mic — and the associated tsunami — hazards. However, the physics governing subduc-
44 tion zone seismicity occurs on a wide range of temporal scales. Tectonic stresses build
45 up over millions of years and are episodically released during earthquakes, which initi-

46 ate, propagate, and stop on time scales smaller than seconds. Capturing the relevant physics
47 across these time scales is computationally and numerically challenging and currently
48 not yet feasible within a single modelling framework.

49 Geodynamic modelling usually tackles large scale, long-term problems, such as sub-
50 duction zone evolution on a lithospheric or global scale over millions of years (see Billen,
51 2008; Gerya, 2011, for an overview). Such models provide insight into the formation and
52 geometry of megathrust faults and the corresponding state of stress (Billen et al., 2003;
53 Goes et al., 2017). However, most geodynamic models do not include elastic rheologies
54 (Patočka et al., 2017) and resolve the physical processes on timescales on the order of
55 thousands of years at most. These restrictions render them unsuitable for studying seis-
56 micity or earthquake rupture dynamics.

57 In contrast, seismic cycle models of the megathrust focus on smaller time scales span-
58 ning thousands of years down to coseismic time scales smaller than seconds (e.g., Rice,
59 1993; Ben-Zion & Rice, 1997; Lapusta et al., 2000; Liu & Rice, 2007; Langer et al., 2010;
60 Kaneko et al., 2011). By modelling both long-term loading of predefined faults and spon-
61 taneous rupture across these faults, seismic cycle models can provide insight into inter-
62 seismic stress build-up, coseismic rupture processes, and postseismic relaxation. How-
63 ever, the majority of seismic cycle models use quasi-static or quasi-dynamic approxima-
64 tions which do not account for the stresses mediated by the emitted seismic waves. No-
65 table fully dynamic exceptions by, for example, Lapusta et al. (2000) and Kaneko et al.
66 (2011), are algorithmically and computationally challenging.

67 Seismic cycle models are commonly limited to predefined faults, which are often
68 simplified to planar geometries. These restrictions may result from the employed numer-
69 ical scheme related to the spatial discretisation or the available computational resources.
70 Furthermore, widely applied seismic cycle methods may inherently only account for ho-
71 mogeneous elastic media (Lapusta et al., 2000). While providing fundamental insight into
72 the mechanics of the earthquake cycle, observations indicate multi-fault geometries and
73 complex lithologies (e.g., Kodaira et al., 2002), which cannot yet be accounted for in state-
74 of-the-art seismic cycle models.

75 Dynamic rupture models are designed to study the dynamics of earthquakes at co-
76 seismic time scales (e.g., Andrews, 1973; Das, 1980; Day, 1982; Madariaga et al., 1998;
77 Oglesby et al., 1998; Ampuero et al., 2002; Dalguer & Day, 2007). Such models provide

78 physically self-consistent earthquake source descriptions by modelling spontaneous fric-
79 tional failure across a predefined fault coupled to seismic wave propagation. By using
80 modern numerical methods and hardware specific software optimisation, dynamic rup-
81 ture simulations can reach high spatial and temporal resolution of increasingly complex
82 geometrical and physical modelling components (Wollherr, Gabriel, & Mai, 2018; Ulrich
83 et al., 2018). In comparison to the aforementioned approaches, such models fully incor-
84 porate inertia effects as well as the non-linear interaction of seismic waves and fault me-
85 chanics governed by friction.

86 However, the dynamic rupture community faces challenges in constraining the ini-
87 tial conditions governing fault stresses and strengths. These are integral ingredients of
88 the dynamic rupture, as they govern the rupture propagation style (e.g., crack- versus
89 pulse-like dynamics and sub- versus supershear rupture speeds), transfers (e.g., dynamic
90 triggering potential), and earthquake arrest (e.g., Kame et al., 2003; Bai & Ampuero,
91 2017).

92 Another important open question is how to constrain the rupture nucleation pro-
93 cess in a physically consistent manner. Dynamic rupture models typically use artificially
94 enforced slip initiation by, e.g., locally reducing the static friction coefficient (Harris, 2004;
95 Harris et al., 2009, 2011, 2018). However, the ensuing rupture is highly sensitive to the
96 chosen nucleation approach and its computational resolution in time and space (Bizzarri,
97 2010; Gabriel et al., 2012, 2013; Galis et al., 2014). Studying earthquake nucleation be-
98 yond ad-hoc approaches will further our understanding of the interaction of megathrust
99 earthquakes, foreshocks and aseismic processes.

100 Ideally, the initial states of stress and fault strength are self-consistent and consis-
101 tent with the geometry and rheology of the subsurface and fault networks. However, due
102 to a lack of constraints, especially on the amplitude of fault-local tractions, fault nor-
103 mal and shear tractions are commonly prescribed as constant or linearly decreasing with
104 depth in dynamic rupture models (Kozdon et al., 2013; Kozdon & Dunham, 2013; Galvez
105 et al., 2014, 2018). Direct measurements of on-fault stresses are difficult to obtain, but
106 inferences from nearby borehole measurements and observations of stress orientations
107 and rotations do provide insight on the shear and normal tractions acting on megath-
108 rusts (Chang et al., 2010; Hardebeck, 2012; Fulton et al., 2013; Hardebeck, 2015). Dy-
109 namic rupture models have successfully incorporated such observations by projecting the

110 inferred regional stress information onto spatially complex fault geometries (Aochi & Fukuyama,
111 2002; Gabriel & Pelties, 2014; Heinecke et al., 2014; Uphoff et al., 2017; Bauer et al., 2017;
112 Madden et al., 2018; Ulrich et al., 2018; Wollherr, Gabriel, & Uphoff, 2018). However,
113 it is difficult to account for variable loading on different fault segments, local litholog-
114 ical heterogeneities, stress and fault roughness, stress interactions between faults and their
115 surroundings, and the different stages of faults within their seismic cycle (Herrendörfer,
116 2018; Romanet et al., 2018).

117 The in situ fault strength is equally hard to constrain. Most studies focus on ex-
118 perimentally constraining the frictional behaviour of rocks at coseismic slip velocities (Dieterich,
119 1979; Ruina, 1983; Di Toro et al., 2011; den Hartog et al., 2012). Drilling experiments
120 and heat flow measurements provide to-scale insight on the frictional strength of megath-
121 rustrs (Fulton et al., 2013). Observational studies indirectly infer the distribution of the
122 pore fluid pressure ratio in subduction zones (Seno, 2009). Various modelling efforts are
123 also aimed at understanding the role of fluids on the strength of the megathrust (Angiboust
124 et al., 2012; Petrini et al., 2017). Despite these advances, a major challenge is the large
125 scaling difference between natural subduction zones, small-scale laboratory experiments,
126 and localised, isolated field measurements.

127 Due to their locations, the exact fault geometry of subduction zones is often un-
128 known. Splay faults are seaward verging crustal faults that splay away from the main
129 subduction megathrust interface at shallow depth. They may rupture in addition to or
130 instead of parts of the megathrust. It has been suggested that these splay faults play an
131 important role during tsunamigenesis, because they could potentially accommodate large
132 vertical displacements (Fukao, 1979). Therefore, several dynamic rupture studies have
133 investigated fault branching and splay fault activation, mostly using simplified geome-
134 tries (Wendt et al., 2009; Tamura & Ide, 2011; DeDontney & Rice, 2012; Li et al., 2014;
135 Madden et al., 2017; Uphoff et al., 2017). Choosing appropriate stress and strength for
136 both the megathrust and the splay fault has been shown to crucially affect branching
137 and dynamic triggering (DeDontney et al., 2012; DeDontney & Hubbard, 2012).

138 “Seismo-thermo-mechanical” models provide insight into complex subduction zone
139 features, such as the role of rheology, temperature, and fault geometry and evolution,
140 including spontaneously evolving splay faults (e.g., van Dinther et al., 2014; Herrendörfer
141 et al., 2015; Corbi et al., 2017; Dal Zilio et al., 2018, 2019; Preiswerk et al., in press; Preuss

142 et al., 2019). These models bridge the time scales of traditional geodynamic and seis-
143 mic cycle models, as initiated by van Dinther, Gerya, Dalguer, Corbi, et al. (2013); van
144 Dinther, Gerya, Dalguer, Mai, et al. (2013). The therein developed two-dimensional model
145 includes the long-term dynamics of subduction, as well as short-term frictional slip tran-
146 sients. However, these models cannot resolve the inertia dynamics of slip events due to
147 numerical restrictions. The minimum resolution is 5 years in time and 500 m in space.
148 The limitations in spatio-temporal resolution were recently overcome for a strike-slip setup
149 (Herrendörfer et al., 2018). Similarly, Sobolev and Muldashev (2017) model time scales
150 down to minutes to resolve postseismic processes in addition to subduction evolution.
151 Nevertheless, the challenge of fully resolving the subduction evolution in combination
152 with rupture dynamics on coseismic time scales remains.

153 To overcome the limitations of each of these approaches, the hereafter presented
154 coupling approach fully resolves the tectonic, seismic cycle (excluding the postseismic
155 phase), and dynamic rupture time scales for the first time by linking a transient slip event
156 of a geodynamic seismic cycle (SC) model to a dynamic rupture (DR) model. By adapt-
157 ing the full outcome of the SC model into initial conditions for the DR model in a phys-
158 ically consistent manner, we provide geometries of the fault and its surroundings, ma-
159 terial properties, and fault stresses and strength. This enables us to study the complex
160 mechanics of subduction zones and megathrust earthquakes in a physically consistent
161 manner.

162 The work presented here is structured as follows. First, we summarise the SC and
163 DR modelling approaches and their respective assumptions in Secs. 2 and 3. We then
164 describe how we couple the geometry, material properties, stresses, and strength condi-
165 tions of a representative SC event to the DR model in Sec. 4, specifically in light of the
166 different set of equations and assumptions both approaches use. We discuss the result-
167 ing state of stress from the long-term subduction evolution in Sec. 5.1 and compare the
168 geodynamic (Sec. 5.2) and dynamic rupture (Sec. 5.3) events in Sec. 5.4. To assess the
169 effect of the heterogeneous, temperature-dependent material properties from the SC model
170 on the dynamic rupture, we conduct a series of models with increasing material complex-
171 ity in Sec. 5.5. In addition to a single megathrust rupture, we investigate the coseismic
172 rupture dynamics along an additional splay fault based on the fault structures visible
173 in the SC model (Sec. 5.6). To ensure that the coupling method is robust, we test the
174 effect of the two main assumptions we made in Sec. 6.1: an idealised Poisson’s ratio gov-

175 erning seismic wave propagation in the DR model (Sec. 6.1.1) and a linear-slip weaken-
 176 ing approximation in the DR model of the rate-weakening friction used in the SC model
 177 (Sec. 6.1.2). In Sec. 6.2, we discuss several possible future lines of work that could ad-
 178 dress the current limitations of our approach. We summarise our most important find-
 179 ings in Sec. 7.

180 **2 Geodynamic seismic cycle model**

181 We use a two-dimensional, visco-elasto-plastic, continuum, seismo-thermo-mechanical
 182 code to solve the long-term dynamics of subduction zone evolution and the subsequent
 183 seismic cycle (Gerya & Yuen, 2007; van Dinther, Gerya, Dalguer, Corbi, et al., 2013; van
 184 Dinther, Gerya, Dalguer, Mai, et al., 2013; van Dinther et al., 2014). First, we briefly
 185 describe the governing equations, rheology, failure criterion, and friction formulation. We
 186 then describe the model setup in Sec. 2.4. A full description of the methods can be found
 187 in Gerya and Yuen (2007) and van Dinther, Gerya, Dalguer, Mai, et al. (2013).

188 **2.1 Governing equations**

189 We solve the following set of conservation equations in a two-dimensional Carte-
 190 sian coordinate system, derived from the principles of conservation of mass (1), momen-
 191 tum (2), and energy (3).

$$\nabla \cdot \mathbf{v} = 0, \quad (1)$$

$$\rho \frac{D\mathbf{v}}{Dt} = \nabla \cdot \boldsymbol{\sigma}' - \nabla P + \rho \mathbf{g}, \quad (2)$$

$$\rho C_p \left(\frac{DT}{Dt} \right) = -\nabla \mathbf{q} + H_a + H_s + H_r. \quad (3)$$

192 All symbols and terms used in these and the following equations are described in Table 1.
 193 The continuity equation (1) assumes an incompressible medium, i.e., Poisson's ratio $\nu =$
 194 0.5. This is valid when pressure and temperature changes are small and therefore only
 195 minimally impact the volume of the material. The energy equation (3) describes con-
 196 ductive ($\nabla \mathbf{q}$) and advective heat transport (within the material derivative $\rho C_p \left(\frac{DT}{Dt} \right)$),
 197 and the internal heat generation due to adiabatic (de)compression H_a , shear heating dur-
 198 ing anelastic deformation H_s , and radioactive heat production H_r .

Table 1. Nomenclature

Symbol	Parameter	Unit
$\dot{\epsilon}_{e,v,p}$	(Elastic, viscous, plastic) Strain rate	s^{-1}
$\dot{\epsilon}_{vp,II}$	Second invariant of the visco-plastic strain rate	s^{-1}
η, η_0	Viscosity, reference viscosity equal to $1/A_d$	Pa s
λ	Pore fluid pressure ratio P_f/P	-
λ_1	First Lamé parameter	Pa
$\mu_{(\text{eff})}^{\text{sc,dr}}$	(Effective) Friction coefficient (SC, DR)	-
$\mu_d^{\text{sc,dr}}$	Dynamic friction coefficient (SC, DR)	-
$\mu_s^{\text{sc,dr}}$	Static friction coefficient (SC, DR)	-
ν	Poisson's ratio	-
ρ, ρ_0	Density, reference density	kg m^{-3}
σ'_{II}	Second invariant of the deviatoric stress tensor	Pa
$\boldsymbol{\sigma}$	Stress tensor	Pa
σ_n	Normal stress	Pa
$\sigma_{\text{yield}}^{\text{sc,dr}}$	Yield stress	Pa
$\sigma_{\text{sliding}}^{\text{sc,dr}}$	Sliding stress	Pa
τ	Shear stress	Pa
χ	Plastic multiplier	s^{-1}
A_D	Pre-exponential factor	$\text{Pa}^{-n} s^{-1}$
C	Cohesion	Pa
C_p	Isobaric heat capacity	$\text{J kg}^{-1} \text{K}^{-1}$
d	Slip	m
D_c	Characteristic slip distance	m
E_a	Activation energy	J mol^{-1}
g	Gravity acceleration	m s^{-2}
G	Shear modulus	Pa
G_{plastic}	Plastic flow potential	Pa
H_a, H_r, H_s	Adiabatic, radioactive and shear heat production	W m^{-3}
n	Stress exponent	-
P	(Solid rock) Pressure	Pa
P_{eff}	Effective pressure	Pa
P_f	Pore fluid pressure	Pa
\mathbf{q}	Heat flux	W m^{-2}
R	Gas constant	$\text{J mol}^{-1} \text{K}^{-1}$
t	Time	s
T	Temperature	K
\mathbf{v}	Velocity	m s^{-1}
v_p	P-wave velocity	m s^{-1}
v_s	S-wave velocity	m s^{-1}
V	Slip rate	m s^{-1}
V_a	Activation volume	$\text{J Pa}^{-1} \text{mol}^{-1}$
V_c	Characteristic velocity	m s^{-1}

199 We use an implicit finite difference scheme on a fully staggered Eulerian grid to solve
 200 for the velocity \mathbf{v} , the solid rock pressure P , and the temperature T (Gerya & Yuen, 2007).
 201 Large deformation is numerically modelled by Lagrangian markers that are advected ac-
 202 cording to their velocity, while keeping track of the rock composition, associated mate-
 203 rial properties, and stress history (see Gerya & Yuen, 2003, and references therein). For
 204 a complete description of all the components of the heat equation used in this model,
 205 we refer to van Dinther, Gerya, Dalguer, Mai, et al. (2013).

206 2.2 Rheology

207 To solve the governing equations, we need constitutive equations that relate the
 208 stress and strain rate. We use a visco-elastic Maxwell rheology in combination with a
 209 frictional plastic slider (Gerya, 2010). The total strain rate is the sum of its viscous, elas-
 210 tic and plastic components:

$$\dot{\boldsymbol{\epsilon}} = \frac{1}{2}(\nabla\mathbf{v} + \nabla\mathbf{v}^T) = \dot{\boldsymbol{\epsilon}}_v + \dot{\boldsymbol{\epsilon}}_e + \dot{\boldsymbol{\epsilon}}_p. \quad (4)$$

211 The viscous strain rate component is

$$\dot{\boldsymbol{\epsilon}}'_v = \frac{1}{2\eta}\boldsymbol{\sigma}', \quad (5)$$

212 where η is the effective viscosity and $\boldsymbol{\sigma}'$ is the deviatoric stress tensor.

213 The elastic strain rate component is described as

$$\dot{\boldsymbol{\epsilon}}'_e = \frac{1}{2G} \frac{D\boldsymbol{\sigma}'}{Dt}. \quad (6)$$

214 It depends on the shear modulus G and the co-rotational stress rate $\frac{D\boldsymbol{\sigma}'}{Dt} = \frac{\boldsymbol{\sigma}'_{t+1} - \boldsymbol{\sigma}'_t}{\Delta t} +$
 215 $\dot{\boldsymbol{\omega}}\boldsymbol{\sigma}' - \boldsymbol{\sigma}'\dot{\boldsymbol{\omega}}$, where $\boldsymbol{\omega} = \frac{1}{2}(\nabla\mathbf{v} - \nabla\mathbf{v}^T)$ is the spin tensor.

216 The plastic strain rate component is described as

$$\dot{\boldsymbol{\epsilon}}'_p = \begin{cases} 0 & \text{if } \sigma'_{\text{II}} < \sigma_{\text{yield}}^{\text{sc}} \\ \chi \frac{\partial G_{\text{plastic}}}{\partial \sigma'_{\text{II}}} & \text{if } \sigma'_{\text{II}} = \sigma_{\text{yield}}^{\text{sc}}. \end{cases} \quad (7)$$

Table 2. Material parameters seismic cycle model

Material	Rock	Flow law ^a	η_0 [Pa ⁿ s]	n [-]	E_a [J mol ⁻¹]	V_a [J Pa ⁻¹]	ρ_0^b [kg m ⁻³]	G^c [GPa]	μ_s [-]	μ_d^i [-]	C [MPa]
Sticky air	-	-	$1.0 \cdot 10^{17}$	1	0	0	1	700	0	0	0
Incoming sediments	Sediments	Wet quartzite	$1.97 \cdot 10^{17}$	2.3	$1.54 \cdot 10^5$	$0.8 \cdot 10^{-5}$	2600	9.7262	0.35 ^d	0.105	2.5
Sediments	Sediments	Wet quartzite	$1.97 \cdot 10^{17}$	2.3	$1.54 \cdot 10^5$	$0.8 \cdot 10^{-5}$	2600	17	0.35 ^d	0.105	2.5
Upper oceanic crust	Basalt	Wet quartzite	$1.97 \cdot 10^{17}$	2.3	$1.54 \cdot 10^5$	$0.8 \cdot 10^{-5}$	3000	38	0.50 ^e	0.150	5 ^j
Lower oceanic crust	Gabbro	Plagioclase	$4.80 \cdot 10^{22}$	3.2	$2.38 \cdot 10^5$	$0.8 \cdot 10^{-5}$	3000	38	0.85 ^f	0.255	15
Upper continental crust	Sandstone	Wet quartzite	$1.97 \cdot 10^{17}$	2.3	$1.54 \cdot 10^5$	$1.2 \cdot 10^{-5}$	2700	34	0.72 ^g	0.216	10
Lower continental crust	Sandstone	Wet quartzite	$1.97 \cdot 10^{17}$	2.3	$1.54 \cdot 10^5$	$1.2 \cdot 10^{-5}$	2700	34	0.72 ^g	0.216	10
Lithospheric mantle	Peridotite	Dry olivine	$3.98 \cdot 10^{16}$	3.5	$5.32 \cdot 10^5$	$0.8 \cdot 10^{-5}$	3300	63	0.60 ^h	0.180	20
Asthenospheric mantle	Peridotite	Dry olivine	$3.98 \cdot 10^{16}$	3.5	$5.32 \cdot 10^5$	$0.8 \cdot 10^{-5}$	3300	72	0.60 ^h	0.180	20
Mantle weak zone	Peridotite	Wet olivine	$5.01 \cdot 10^{20}$	4.0	$4.70 \cdot 10^5$	$0.8 \cdot 10^{-5}$	3300	63	0.10	0.03	20

See van Dinther, Gerya, Dalguer, Mai, et al. (2013) for parameters related to the energy equation (3). Values obtained from: ^aRanalli (1995) unless otherwise stated; ^bTurcotte and Schubert (2002); ^cBormann et al. (2012); ^dDen Hartog et al. (2012); ^eDi Toro et al. (2011); ^fTsutsumi and Shimamoto (1997); ^ge.g., Dieterich (1978); Chester and Higgs (1992); Di Toro et al. (2011); ^hDel Gaudio et al. (2009); ⁱfriction coefficient decreases to 30% of its initial value according to Di Toro et al. (2011); ^jSchultz (1995).

217 In this plastic flow rule, G_{plastic} is the plastic potential of yielding material and χ is the
 218 plastic multiplier, which connects the components of the plastic strain rate with the lo-
 219 cal stress distribution σ'_{II} .

220 We consider dislocation creep with a non-linear viscosity η that depends on the sec-
 221 ond invariant of the stress tensor σ'_{II} (e.g., Ranalli, 1995):

$$\eta = \left(\frac{1}{\sigma'_{II}}\right)^{n-1} \cdot \frac{1}{2A_D} \cdot \exp\left(\frac{E_a + PV_a}{RT}\right), \quad (8)$$

222 where R is the gas constant and n , A_d , E_a , and V_a are material dependent viscous pa-
 223 rameters (Table 1). Values for the material parameters for each rock type are constrained
 224 by experimental studies and can be found in Table 2.

225 **2.3 Failure criterion and friction formulation**

226 Brittle behaviour is characterised by Drucker-Prager plasticity (Drucker & Prager,
 227 1952), which is commonly used in geodynamics (e.g., Kaus, 2010; Buiter et al., 2016).
 228 In this yield criterion, the second invariant of the deviatoric stress $\sigma'_{II} = \sqrt{\sigma'^2_{xx} + \sigma'^2_{xz}}$
 229 at a point in the rock is compared to the strength (or yield stress) $\sigma^{\text{sc}}_{\text{yield}}$ of the rock. Plas-
 230 tic failure in the form of spontaneous brittle instabilities occurs when the stress reaches
 231 the rock's strength. The strength of a rock depends on its cohesion C , its friction coef-
 232 ficient μ^{sc} , and the effective pressure P_{eff} , according to

$$\sigma^{\text{sc}}_{\text{yield}} = C + \mu^{\text{sc}} P_{\text{eff}}, \quad (9)$$

233 with P_{eff} defined as

$$P_{\text{eff}} = P - P_f = (1 - \lambda)P, \quad (10)$$

234 where P_f is the pore fluid pressure, such that λ is the pore fluid pressure ratio P_f/P .
 235 We solve a simplified formulation of fluid flow processes including metamorphic (de)hydration
 236 reactions and compaction (e.g., Gerya & Meilick, 2011). These processes are driven by
 237 pressure, depth, and temperature.

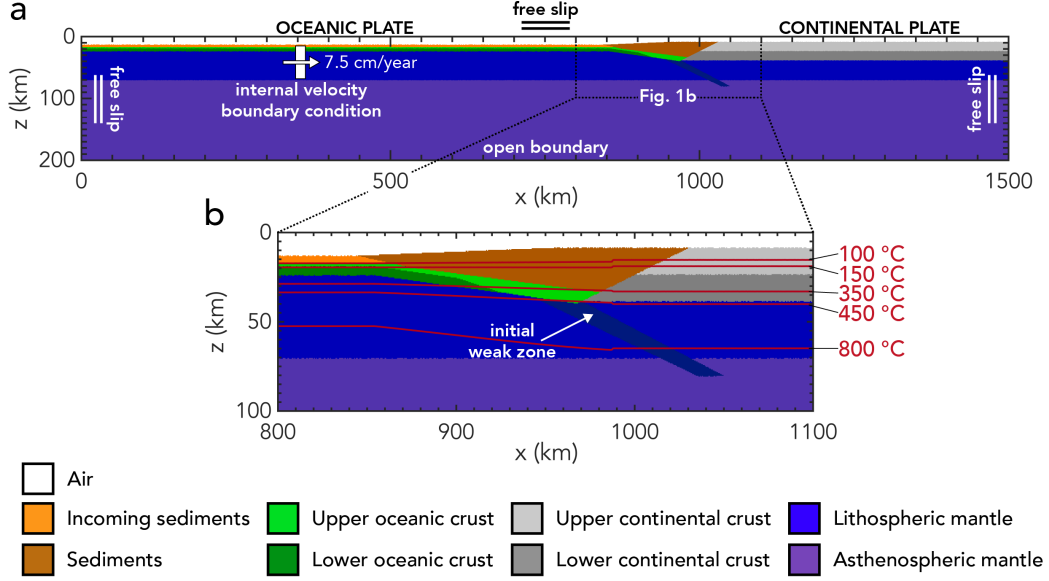


Figure 1. Complete (a) and zoomed (b) model setup of the geodynamic seismic cycle model with lithology (in colour, see key), isotherms (red), and boundary conditions (white).

238 We use a strongly slip rate-dependent friction formulation (van Dinther, Gerya, Dalguer,
 239 Corbi, et al., 2013) in which the friction coefficient μ^{sc} drops non-linearly from the static
 240 friction coefficient μ_s^{sc} to the dynamic friction coefficient μ_d^{sc} with increasing slip rate V ,
 241 according to

$$\mu^{\text{sc}} = \frac{V_c \mu_s^{\text{sc}} + V \mu_d^{\text{sc}}}{V_c + V}, \quad (11)$$

242 where V_c is the characteristic velocity at which half of the friction drop occurs. The visco-
 243 plastic slip rate V is derived from the visco-plastic strain rate according to

$$V = \dot{\epsilon}'_{vp,II} \Delta x, \quad (12)$$

244 where Δx is the minimum grid size. This results in an inherently grid size dependent
 245 slip rate.

246 **2.4 Geodynamic seismic cycle model setup**

247 We use the two-dimensional setup of a trench-normal section of the Southern Chilean
 248 subduction zone where the oceanic Nazca plate subducts beneath the continental South
 249 American plate in a $1500 \times 200 \text{ km}^2$ box (Fig. 1; van Dinther, Gerya, Dalguer, Mai,
 250 et al., 2013). The model has a minimum grid size of 500 m in the high resolution area
 251 around the megathrust interface, which increases to 2000 m at the edges of the model.
 252 This results in a grid of 1654×270 nodes. A total of ~ 54.3 million markers is used
 253 to advect the different materials and their physical properties.

254 The top of the Nazca plate includes a 4 km incoming sediment layer to create a large
 255 accretionary prism in which splay geometries develop. In addition to the sediment layer,
 256 the oceanic Nazca plate consists of a 2 km thick basaltic upper oceanic crust and a 5 km
 257 thick gabbroic lower oceanic crust. The initial accretionary wedge consists of sediments
 258 and the continental South American plate consists of a 15 km thick sandstone upper con-
 259 tinental crust and a 15 km thick sandstone lower continental crust. We use a wet quartzite
 260 flow law (Ranalli, 1995) for the continental crust, the sediments, and the upper oceanic
 261 crust; and we use a plagioclase flow law (Ranalli, 1995) for the lower oceanic crust. The
 262 two plates overlie an anhydrous, peridotitic mantle that is approximated with a dry olivine
 263 flow law. We use laboratory-derived material parameters for the different rheologies as
 264 described in van Dinther, Gerya, Dalguer, Mai, et al. (2013), but update cohesion val-
 265 ues constrained by e.g., Ranalli (1995); Schultz (1995), and shear modulus values follow-
 266 ing Bormann et al. (2012) (Table 2).

267 We consider long-term fluid flow with a constant pore fluid pressure ratio. At the
 268 start of the model, the ocean floor sediments and oceanic crust contain water. Regions
 269 within 2 km of fluids have an increased pore fluid pressure ratio $\lambda = 0.95$, whereas for
 270 dry rocks, the pore fluid pressure ratio $\lambda = 0$. This value of the increased pore fluid pres-
 271 sure ratio is based on observations for Southern Chile (Seno, 2009). The highly over-pressurised
 272 pore fluids are required to sustain subduction along a shallow megathrust and obtain rea-
 273 sonable seismic cycle characteristics (van Dinther, Gerya, Dalguer, Mai, et al., 2013). An
 274 increased pore fluid pressure ratio results in decreased rock strength (Eq. 9), so the pres-
 275 ence of fluids is of major importance for the nucleation and propagation of earthquakes
 276 in these models. The model does not account for plate (de)hydration reactions, erosion
 277 processes, and serpentinitisation.

278 The seismogenic zone in the SC model develops with the temperature profile of the
 279 slab. We impose a velocity-weakening regime when the temperature is higher than 150°C
 280 (see Table 2 for lithology-dependent velocity-weakening friction parameters; Blanpied
 281 et al., 1995; van Dinther, Gerya, Dalguer, Mai, et al., 2013). Between 100°C and 150°C,
 282 there is a transition from velocity-strengthening to velocity-weakening behaviour. The
 283 exact switch from velocity-weakening to velocity-strengthening behaviour occurs between
 284 the 104°C and 134°C isotherm, depending on rock type and slip rate. We impose a velocity-
 285 strengthening regime in the shallow part of the domain when the temperature of the slab
 286 is lower than 100°C with constant friction parameters for all rock types with a static fric-
 287 tion coefficient $\mu_s^{sc} = 0.35$, a maximum dynamic friction coefficient $\mu_d^{sc} = 0.875$, and
 288 a characteristic slip velocity $V_c = 2 \cdot 10^{-9}$ m/s (see van Dinther, Gerya, Dalguer, Mai,
 289 et al., 2013, and references therein). The downdip limit of the seismogenic zone forms
 290 self-consistently with respect to the brittle-ductile transition that is governed by the temperature-
 291 dependent viscosity.

292 During the first stage of the model the time step is 1000 years and a suitable sub-
 293 duction geometry is obtained. After 3.6 million years, the time step is gradually reduced
 294 to 5 years, which results in the start of the seismic cycle phase of the model after 4.0 mil-
 295 lion years. We run the seismic cycle phase of the model for ~ 30 thousand years, during
 296 which the stresses are initially adapted to seismic cycles. Then, our long run time en-
 297 sures that we have a long enough observation time to produce robust seismic cycle statis-
 298 tics (van Dinther, Gerya, Dalguer, Mai, et al., 2013).

299 We use a sticky air approach to approximate a free surface (Cramer et al., 2012).
 300 Free slip boundary conditions are used at the top and sides of the model and we have
 301 an open boundary condition at the bottom. An internal velocity boundary condition ap-
 302 plied to the subducting slab ensures that subduction is initiated and sustained. The ini-
 303 tial and boundary conditions we use are the same as in van Dinther, Gerya, Dalguer, Mai,
 304 et al. (2013) and are explained in detail in Appendix A, Appendix B and Fig. 1.

305 **3 Dynamic rupture model**

306 We use the two-dimensional version of the software package SeisSol ([http://www](http://www.seissol.org)
 307 [.seissol.org](http://www.seissol.org)) to solve for earthquake source dynamics coupled to seismic wave prop-
 308 agation (Dumbser & Käser, 2006; de la Puente et al., 2009; Pelties et al., 2014). Seis-

309 Sol is specifically suited for handling complex geometries due to the use of unstructured
 310 tetrahedral computational meshes.

311 In the following, we shortly summarise the governing equations and frictional fail-
 312 ure criterion. The reader is referred to Dumbser and Käser (2006) for a full description
 313 of the numerical method and to de la Puente et al. (2009) for details on the implemen-
 314 tation of rupture dynamics as an internal boundary condition.

315 3.1 Governing equations

316 SeisSol solves the elastic wave equation in a two-dimensional Cartesian coordinate
 317 system without external body forces in an isotropic, compressible medium:

$$\rho \frac{\partial \mathbf{v}}{\partial t} = \nabla \cdot \boldsymbol{\sigma} \quad (13)$$

$$\dot{\boldsymbol{\epsilon}}_e = \frac{1}{2G} \frac{\partial \boldsymbol{\sigma}}{\partial t} - \frac{\lambda_1}{2G} \nabla \cdot \mathbf{v} \quad (14)$$

318 Eq. 13 is the equation of motion (compare to Eq. 2) and Eq. 14 is the constitutive re-
 319 lation derived from Hooke’s law that relates the strain rate to stresses for an elastic, isotropic
 320 material (compare to Eq. 6). Since we only consider an elastic medium in the DR model,
 321 the elastic strain rate $\dot{\boldsymbol{\epsilon}}_e$ equals the total strain rate $\dot{\boldsymbol{\epsilon}} = \frac{1}{2}(\nabla \mathbf{v} + \nabla \mathbf{v}^T)$ (compare to
 322 Eq. 4). λ_1 and G are the Lamé constants, which determine the Poisson’s ratio of the model
 323 (Secs. 4.2 and 6.1.1).

324 To discretise this set of equations in space, SeisSol uses a Discontinuous Galerkin
 325 (DG) method with a Godunov upwind flux, which represents the solution as an exact
 326 Riemann problem at the discontinuity between element interfaces (Dumbser & Käser,
 327 2006; de la Puente et al., 2009). Due to the use of triangular mesh elements, this approach
 328 is particularly suited for the discretisation of complex geometries like shallow dipping
 329 subduction zones, topography or bathymetry. For the discretisation in time, SeisSol uses
 330 an Arbitrary high-order DERivative (ADER) method (Dumbser & Käser, 2006).

331 Due to the dissipative behaviour of the numerical upwind flux used by SeisSol, spu-
 332 rious high frequency oscillations are subdued in the vicinity of the fault (de la Puente
 333 et al., 2009; Pelties et al., 2014; Wollherr, Gabriel, & Uphoff, 2018). SeisSol is verified
 334 with a wide range of two-dimensional and three-dimensional community benchmarks,

335 including strike-slip, dipping and branching fault geometries, laboratory derived friction
 336 laws, as well as heterogeneous on-fault initial stresses and material properties (de la Puente
 337 et al., 2009; Pelties et al., 2012, 2014; Wollherr, Gabriel, & Uphoff, 2018) in line with the
 338 SCEC/USGS Dynamic Rupture Code Verification exercises (Harris et al., 2011, 2018).

339 **3.2 Failure criterion and friction formulation**

340 We incorporate frictional failure as an internal boundary condition of the element
 341 edges associated with the fault, which is meshed explicitly. Fault slip in the DR model
 342 is therefore restricted to this fault line in contrast to the SC model where the entire do-
 343 main is theoretically allowed to slip.

344 To check the Coulomb failure criterion, the stress tensor, which consists of the ini-
 345 tial stress and any subsequent stress change, is rotated into the fault coordinate system
 346 defined by the normal and tangential vectors of each fault point. The DR model com-
 347 pares the absolute shear stress $|\tau|$ on the fault to the fault yield strength $\sigma_{\text{yield}}^{\text{dr}}$

$$\sigma_{\text{yield}}^{\text{dr}} = C + \mu_s^{\text{dr}} \sigma_n. \quad (15)$$

348 It consists of the fault cohesion C , the static friction coefficient μ_s^{dr} , and the normal stress
 349 σ_n (compare to Eq. 9). If the shear stress overcomes the fault strength, the fault fails
 350 and its strength becomes $\sigma_{\text{sliding}}^{\text{dr}}$:

$$\sigma_{\text{sliding}}^{\text{dr}} = \mu^{\text{dr}} \sigma_n. \quad (16)$$

351 During sliding, the friction coefficient μ^{dr} is governed by a linear slip weakening friction
 352 law (Ida, 1973). For this constitutive law, μ^{dr} decreases linearly from its static value μ_s^{dr}
 353 to its dynamic value μ_d^{dr} with slip distance Δd over a specified critical slip distance D_c ,
 354 i.e.

$$\mu^{\text{dr}} = \begin{cases} \mu_s^{\text{dr}} - \frac{\mu_s^{\text{dr}} - \mu_d^{\text{dr}}}{D_c} \Delta d & \text{if } \Delta d < D_c \\ \mu_d^{\text{dr}} & \text{if } \Delta d \geq D_c. \end{cases} \quad (17)$$

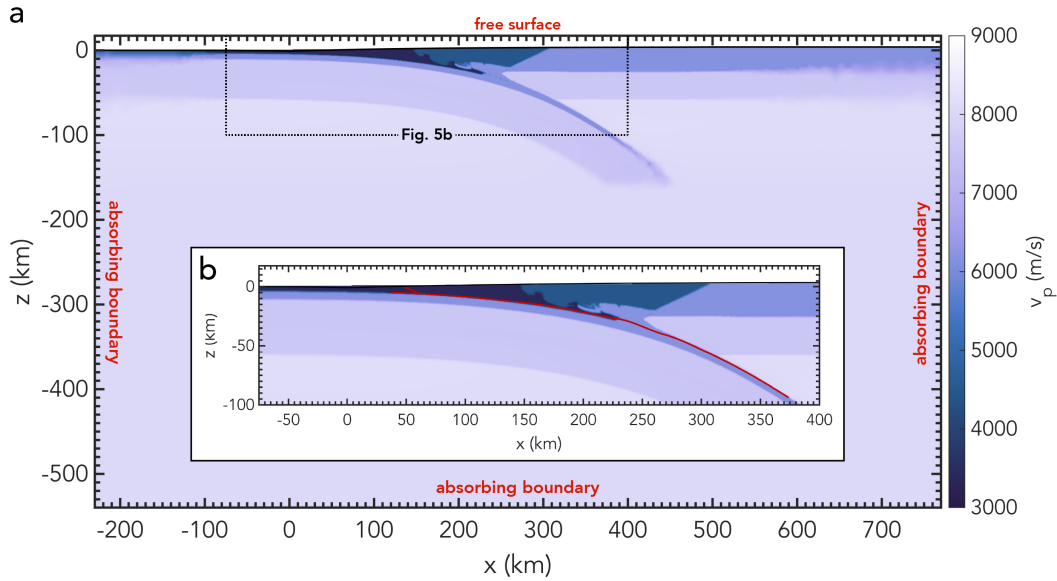


Figure 2. Complete (a) and zoomed (b) model setup of the dynamic rupture model with P-wave velocity v_p (in colour; Table 3), boundary conditions (red) and megathrust and splay fault geometry (red lines). The splay fault is always explicitly meshed in the DR model, but the frictional boundary condition on the splay fault is only activated for the model in Sec. 5.6.

3.3 Dynamic rupture model setup

The DR modelling domain is a 575 km wide and 169 km deep subsection of the SC domain (Fig. 2). We copy the SC values at the boundaries of this domain to extend the DR simulation domain to 1000 km width and 544 km depth to avoid artificial wave reflections from the boundaries. Copying the values is necessary, because of the limited depth of the SC model and the interference of boundary conditions with the material parameters and physical variables close to the domain edges. The fault geometry is extracted from the SC model according to the region of highest visco-plastic strain rate during the SC coupling event (see Sec. 4.3).

For the dynamic rupture simulations we use a 6th order spatial and temporal discretisation. The nodal grid size at the fault is 200 m and is increased away from the fault, with a maximum grid size of 50 km at the domain boundaries. Note that the fault is additionally subsampled by six Gaussian integration points which increases the resolution on the fault to 33.3 m. The corresponding mesh consists of 543'048 elements.

Table 3. Seismic velocities dynamic rupture model

Material	v_p [m s ⁻¹]	v_s [m s ⁻¹]
Incoming sediments	3350	1934
Sediments	4429	2557
Upper oceanic crust	6164	3559
Lower oceanic crust	6164	3559
Upper continental crust	6146	3549
Lower continental crust	6146	3549
Lithospheric mantle	7568	4369
Asthenospheric mantle	8090	4671

369 To ensure stability of the numerical scheme, the time step is calculated in depen-
370 dence of the Courant-Friedrichs-Lewy criterion using $C_{CFL} = 0.5$ (de la Puente et al.,
371 2009), the minimum insphere over all mesh elements, and the fastest wave speed v_p . This
372 leads to a time step of $7.5 \cdot 10^{-5}$ s.

373 Element-wise values for friction parameters, initial stress and strength, and rock
374 properties with seismic velocities listed in Table 3, are obtained from the SC model as
375 described in Sec. 4.

376 We use a free surface boundary condition, which sets shear and normal stresses to
377 zero in the absence of external forces. Additionally, the model uses absorbing boundary
378 conditions which reduce the reflections of outgoing waves at the domain boundaries (Dumbser
379 & Käser, 2006).

380 4 Coupling method

381 In this section, we discuss the resulting long-term seismicity characteristics of the
382 SC model and how we choose an event from the SC model to couple to the DR model.
383 We then show how we couple the material properties of the domain, the fault geome-
384 try, friction parameters, and stress in the two modelling approaches. The full SC results
385 used for coupling to the dynamic rupture model are included in the Supporting Infor-
386 mation and can be used as input for other dynamic rupture models.

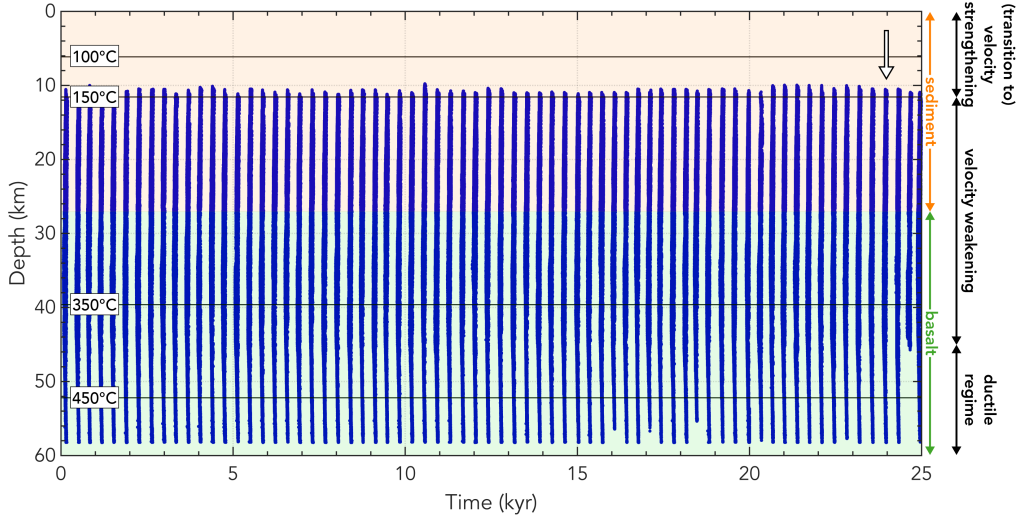


Figure 3. Space-time evolution of the SC model of subduction zone seismicity. Each dot (closely clustered together to form lines) represents a marker that satisfies our Rupture Detector Algorithm thresholds (see text; Dal Zilio et al., 2018). The event that we use as the SC coupling event for our SC to DR coupling is indicated by the arrow. Frictional regimes dependent on temperature are indicated with corresponding isotherms (solid black lines). Background colours represent the rock type through which the fault is going.

387 **4.1 Long-term seismic cycle characteristics and selection of coupling time** 388 **step**

389 In the seismic cycle phase, we observe 70 spontaneous quasi-periodic megathrust
390 events (Fig. 3). To quantify their characteristics we apply a minimum slip rate thresh-
391 old of $2.5 \cdot 10^{-9}$ m/s and a minimum stress drop threshold of 0.4 MPa on all markers
392 (Dal Zilio et al., 2018). Most events rupture almost the entire megathrust apart from
393 the shallow, velocity-strengthening part. The exact rupture path is different for each event,
394 because of the different stress and strain distributions for each event in the broad sub-
395 duction channel and accretionary wedge. This is particularly true in the downdip region
396 of the seismogenic zone where the rupture paths sometimes deviate from the rock inter-
397 faces. In the shallow part of the subduction zone, the sediments are favoured over the
398 basalt for rupture propagation, due to their lower strength (Table 2). The average re-
399 currence interval of the megathrust events is approximately 270 years, which is in line
400 with estimates of the recurrence interval in Southern Chile (e.g., Cisternas et al., 2005).

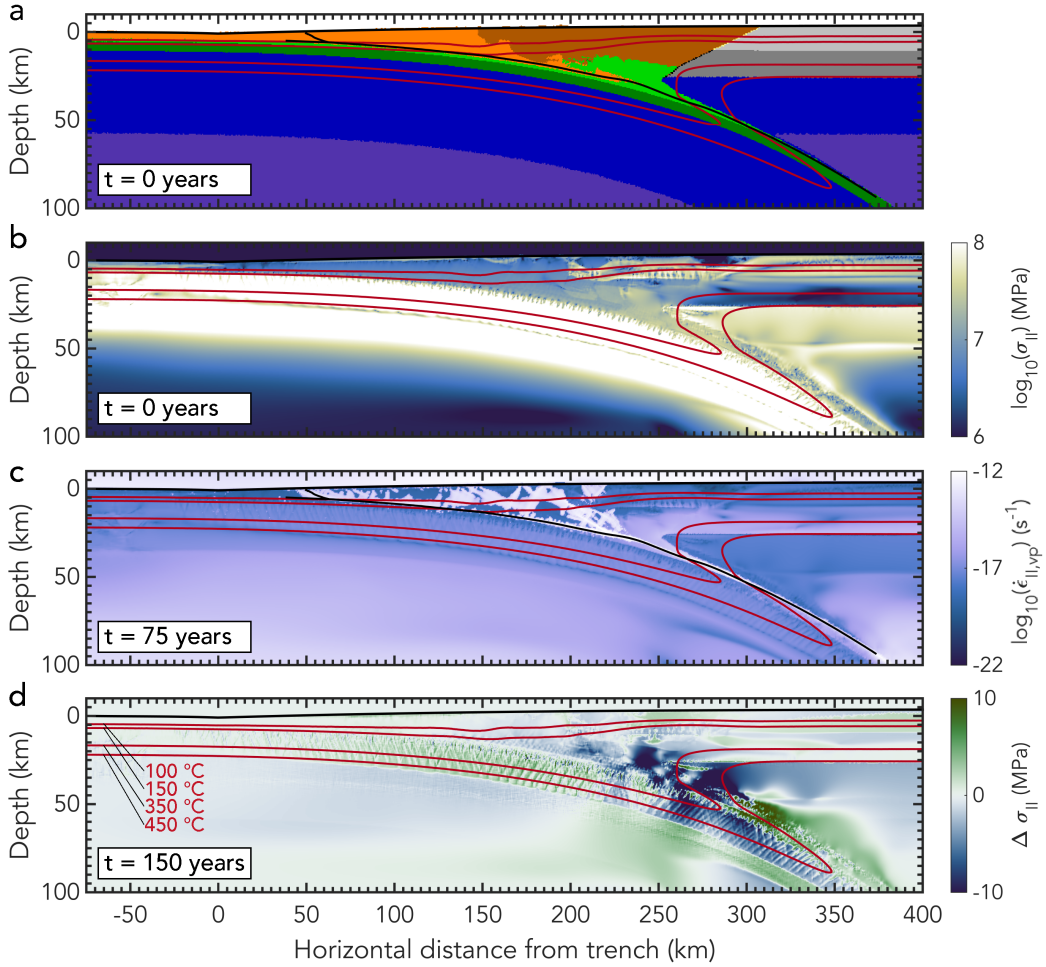


Figure 4. Representative coupling event of the geodynamic seismic cycle model. (a) Lithological structure after 4 Myr (compare to Fig. 1) at the start of the event ($t = 0$ years) with the fault indicated in black. (b) Initial stress used as input for the DR model. (c) Strain rate during the event at 75 years from the start of the event with the fault indicated in black. (d) Stress change with respect to the initial stress in (b) towards the end of the event 150 years from the start. Isotherms that define the frictional regimes and hence seismogenic zone are indicated in red. The boundary between rocks and sticky air is highlighted with a thick solid black line. Note that the x - and z -axes are shifted with respect to Fig. 1 such that the trench has coordinates (0,0).

401 We choose the rupture indicated by the arrow in Sec. 3 as the SC coupling event
 402 that we import to the dynamic rupture model. The chosen event is representative for
 403 other events in terms of its duration and stress drop and it has a smooth rupture path.
 404 The geometry resulting from ~ 4 Myr subduction consists of a large accretionary wedge
 405 created by the incoming sediments and a slab with an average dip of 14° (Fig. 4a). At
 406 the initiation of the rupture, stress has built up during the interseismic stage in the lower
 407 part of the seismogenic zone (Fig. 4b). Like all other events in the SC model, this event
 408 also results in a lot of yielding in the shallow part of the accretionary wedge as shown
 409 by the strain rate localisation in Fig. 4c. This large yielding region represents the large-
 410 scale failure of the unconsolidated accretionary wedge, which contains multiple possible
 411 splay fault geometries. Although the localisation of strain on the splay faults and the
 412 megathrust is simultaneous, the splay faults are not detected as part of an event, because
 413 of their lower slip velocity. The resulting stress change of the SC event in Fig. 4d shows
 414 a stress drop in the subduction channel, particularly near the downdip limit of the seis-
 415 mogenic zone.

416 We need to choose the coupling time step of the SC coupling event for which we
 417 import the conditions from the SC model to the DR model as initial conditions. For this
 418 coupling time step we export the rock properties, friction coefficient and stresses to the
 419 DR model, as discussed in the following sections. We also use this time step as the start
 420 of the SC event, so that we can use it and its subsequent time steps that comprise the
 421 entire SC event to determine the fault geometry and dynamic friction coefficient.

422 We select the first time step of the coupling event in the SC model for which nu-
 423 cleation and subsequent propagation of the rupture occurs spontaneously in the DR model
 424 in order to stay as close to the SC model as possible. This time step corresponds to the
 425 time step at which failure occurs in the SC model on two adjacent fault points.

426 **4.2 Lithological structure**

427 Density, shear modulus, and cohesion are directly transported into the DR model.
 428 The sticky air material, which is used for the free surface approximation in the SC model,
 429 does not enter the DR model, which has a true free surface boundary condition. To pro-
 430 vide the DR model with a smooth surface and purely rock-related properties (i.e., no sticky
 431 air), we first approximate the air-rock boundary of the SC model with a 3rd order poly-

432 nominal that is used as the free surface geometry of the DR model. The sticky air val-
 433 ues are then replaced by the values of the underlying rock to prevent any of the sticky
 434 air properties to enter the DR model.

435 The SC model assumes incompressible materials, i.e., Poisson's ratio $\nu = 0.5$. In
 436 the DR model, the material is compressible, so $\nu \neq 0.5$. We choose $\nu = 0.25$ to cal-
 437 culate the first Lamé parameter λ_1 from the shear modulus G in the SC model. This value
 438 of Poisson's ratio is based on the simplifying assumption that rocks can be treated as
 439 Poisson solids with $\lambda_1 = G$ (Stein & Wysession, 2009). We discuss possible variations
 440 of Poisson's ratio and its influence on the rupture dynamics in Sec. 6.1.

441 4.3 Fault geometry

442 As the fault geometry in the DR model needs to be predefined, we have to define
 443 a localised, infinitely thin fault line from the SC model. Therefore, we look at the cou-
 444 pling time step of Sec. 4.1 and the 43 subsequent time steps that make up the SC event.
 445 We pick the z -coordinate with the highest visco-plastic strain rate during the entire SC
 446 slip event for each nodal x -coordinate (Fig. 4c). We smooth the fault with a moving av-
 447 erage low-pass filter scheme with a span of 25 points. This ensures that the nucleation
 448 region is correctly represented in the fault geometry.

449 The SC fault geometry reveals that a shallow splay fault is preferred over the megathrust
 450 in the velocity-strengthening region (Figs. 4 and 2). For simplicity, our models ini-
 451 tially only contain the megathrust, which is manually extended by adding ~ 25 km up-
 452 dip of the fault with the constant dip from the shallowest part of the megathrust. The
 453 total length of the megathrust is then 351.3 km with an average dip of 14.3° and a min-
 454 imum and maximum dip of 2.3° and 34.4° , respectively. The splay fault is connected to
 455 the megathrust at $x = 24.5$ km along the megathrust. It has a length of 14.6 km with
 456 an average dip of 21.1° and a minimum and maximum dip of 8.1° and 36.8° , respectively.
 457 This splay fault is included in the mesh for all DR models to ensure that the results of
 458 adding a splay fault in Sec. 5.6 are not influenced by any changes in the mesh. In Sec. 5.6,
 459 the frictional boundary condition on the splay fault is activated, so that slip on the splay
 460 fault is theoretically possible. In all other models, the frictional boundary condition on
 461 the splay fault is turned off.

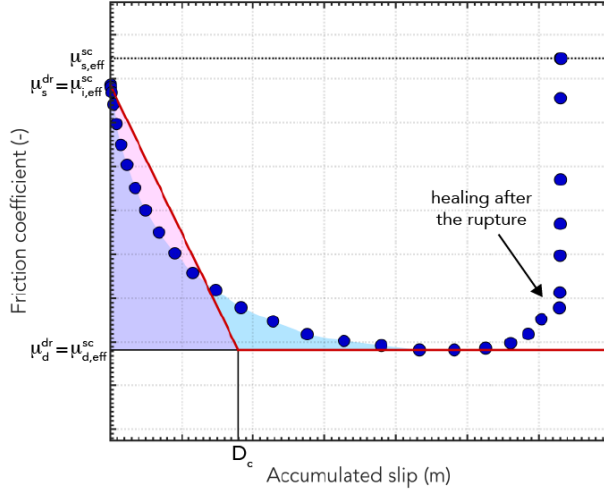


Figure 5. Illustration of the linear slip weakening approximation of rate-dependent friction for one fault point. Each blue dot represents the effective friction coefficient and corresponding accumulated slip for one time step of the SC model during the entire rupture. The final picked μ_s^{dr} , μ_d^{dr} , and D_c are indicated by solid black lines. The final linear slip weakening approximation is indicated in red. D_c is calculated by ensuring that the friction drop during slip of the linear slip weakening law (pink area underneath red line) equals the friction drop during slip of the rate-dependent friction law (blue area underneath blue dots). The area is purple where these two areas overlap. Note that the static friction coefficient of the DR model is not necessarily equal to that of the SC model, but instead equals the SC friction coefficient at the start of the event $\mu_{i,eff}^{sc}$.

462 4.4 Friction parameters

463 The presence of pore fluids, with a pore fluid pressure ratio $\lambda = 0.95$, reduces the
 464 effective friction coefficient in the SC model (Sec. 2.4). To account for the fluids present
 465 in the SC model, we use an effective friction coefficient determined by $\mu^{dr} = \mu_{eff}^{sc} = (1 -$
 466 $\lambda)\mu^{sc}$ for both the static and dynamic friction coefficients μ_s^{dr} and μ_d^{dr} , respectively. The
 467 effective friction coefficients range from 0.028 to 0.005 and are in line with theoretical
 468 estimates (e.g., Wang & Hu, 2006) and experiments (e.g., Kopf & Brown, 2003; Ujiie et
 469 al., 2013).

470 We import the current friction coefficient μ_i^{sc} of our coupling time step as the ini-
 471 tial, static friction coefficient for the DR model. We use the minimum friction coefficient
 472 μ_d^{sc} that is reached during the event in the SC model as the DR dynamic friction coef-
 473 ficient. The corresponding characteristic slip distance D_c is then calculated such that

474 the area of the strength drop during slip of the linear slip weakening law equals the area
 475 of the strength drop during slip of the rate-dependent friction law:

$$D_c = \frac{2}{\mu_s^{\text{dr}} - \mu_d^{\text{dr}}} \sum_{t=1}^{t_{\text{max}}} (d_t - d_{t-1}) \cdot \left(\mu_{\text{eff},t}^{\text{sc}} + \frac{1}{2} \mu_{\text{eff},t-1}^{\text{sc}} - \mu_d^{\text{dr}} \right). \quad (18)$$

476 Here, $t = 0$ is the coupling time step (Sec. 4.1), t_{max} is the time step in the SC model
 477 at which the lowest friction coefficient is obtained, d is the accumulated slip for a given
 478 point in time and the SC friction coefficients are the effective friction coefficients. Also
 479 note that $\mu_d^{\text{dr}} = \mu_{d,\text{eff}}^{\text{sc}}$. Fig. 5 illustrates this friction law approximation for one fault
 480 point, with the data from the SC model plotted as blue dots and the corresponding lin-
 481 ear slip weakening approximation for the DR model in red.

482 Using this approach, we get a self-consistent approximation in the DR model of the
 483 velocity-strengthening behaviour in the shallow part of the SC model by having $\mu_d^{\text{dr}} >$
 484 μ_s^{dr} .

485 We use trilinear interpolation to map the friction coefficients and the cohesion element-
 486 wise onto the additional sub-elemental Gaussian integration points along all element edges
 487 hosting a dynamic rupture boundary condition.

488 4.5 State of stress

489 The SC model uses deviatoric stresses σ' , like many other geodynamic models, whereas
 490 the DR model uses non-deviatoric stresses. The two models also use different sign and
 491 coordinate conventions (more details in the Supporting Information), so the stresses from
 492 the SC model need to be converted to the conventions of the DR model.

493 First, the deviatoric stresses σ'^{sc} of the SC model are converted to non-deviatoric
 494 stresses σ^{sc} according to

$$\sigma^{\text{sc}} = \begin{pmatrix} \sigma_{xx}^{\text{sc}} & \sigma_{xz}^{\text{sc}} \\ \sigma_{xz}^{\text{sc}} & \sigma_{zz}^{\text{sc}} \end{pmatrix} = \begin{pmatrix} \sigma_{xx}'^{\text{sc}} - P & \sigma_{xz}^{\text{sc}} \\ \sigma_{xz}^{\text{sc}} & -\sigma_{xx}'^{\text{sc}} - P \end{pmatrix}, \quad (19)$$

495 where P is the solid rock pressure.

496 Besides that, we need to take into account the different coordinate systems with
 497 the z -axis pointing downwards for the SC model and upwards for the DR model. The

498 two models also have opposite stress conventions for both the diagonal and shear com-
 499 ponents of the stress tensor (see the Supporting Information for details). To account for
 500 this, we use the following stress tensor as input for the DR model:

$$\sigma^{dr} = \begin{pmatrix} -\sigma_{xx}^{sc} & \sigma_{xz}^{sc} \\ \sigma_{xz}^{sc} & -\sigma_{zz}^{sc} \end{pmatrix}. \quad (20)$$

501 We use the same trilinear interpolation scheme used for the friction parameters to
 502 map the SC stress field onto the DR fault. Based on the fault orientation, the shear and
 503 normal tractions on the fault are then determined to evaluate the yield criterion in the
 504 DR model (Eq. 15).

505 5 Results and analysis

506 In this section, we first describe the on-fault stress state that results from the SC
 507 model in Sec. 5.1. We then describe the results from the SC event (Sec. 5.2) and the cor-
 508 responding DR rupture (Sec. 5.3) in detail and compare them (Sec. 5.4). In Sec. 5.5, we
 509 study the effect of complex lithological structures on the resulting rupture through a se-
 510 ries of increasingly complex models studies. Lastly, we analyse how a splay fault affects
 511 the dynamic rupture in Sec. 5.6.

512 5.1 Long-term constrained state of stress of the megathrust

513 Fig. 6 shows the variability of the on-fault stress σ'_{II} which is used in the SC fail-
 514 ure criterion (Eqs. 7 and 9) for the 14 events during the last 5000 years of simulation time
 515 of the SC model. It is calculated by obtaining the minimum and maximum stress for each
 516 fault point from 10 time steps around the nucleation time. For simplicity, we used the
 517 fault geometry of the coupled SC event (Sec. 4.3), although the actual fault geometries
 518 of other events might deviate from that of the coupled event (van Dinther, Gerya, Dalguer,
 519 Mai, et al., 2013). We visualise variables of the SC model on the discrete DR fault (Sec. 4.3)
 520 by using the values of the neighbouring grid cell with the highest strain rate for each fault
 521 point, which approximates the fault of the SC event optimally. As the rupture path changes
 522 for each event, this leads to slight deviations in individual stress profiles, but it does not
 523 change the overall stress variability, i.e., the minimum and maximum possible initial stress
 524 at a fault point.

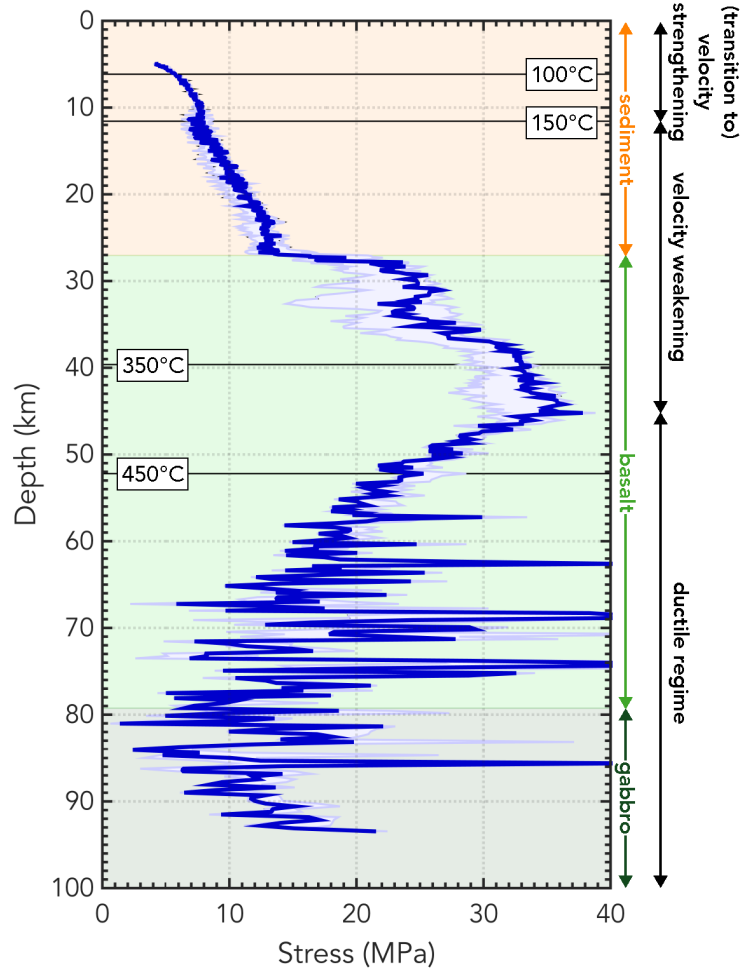


Figure 6. Variability of the stress σ'_{II} at the time of nucleation indicated by the light blue shaded area with the initial stress of the reference model indicated by the blue line. Frictional regimes dependent on temperature are indicated with corresponding isotherms (solid black lines). Background colours represent the rock type through which the fault is going.

525 The stress profiles in Fig. 6 all show a similar trend in terms of stress distribution
 526 along the fault with depth and the amount of stress heterogeneity. There is no stress vari-
 527 ability in the upper part of the sediments where the velocity-strengthening regime dom-
 528 inates. This is due to the fact that the events do not propagate on this part of the fault,
 529 but instead choose a splay fault over the megathrust in the velocity-strengthening re-
 530 gion (Sec. 4.3). There is little variation in the velocity-weakening regime of the sediments.
 531 The stress variability becomes larger in the basalt with the maximum difference in nu-
 532 cleation stress at a given fault point being 11.5 MPa. There is a peak in the stresses at
 533 the downdip end of the seismogenic zone below the 350°C isotherm. This is the nucle-
 534 ation region of most of the SC events. Here, the stress build-up is largest, because the
 535 differential displacement between the locked seismogenic zone and the creeping viscous
 536 domain is largest. In the ductile regime starting at 45 km depth, the stresses decrease
 537 by viscous relaxation related to the dislocation creep (Fig. 7). The spontaneous brittle-
 538 ductile transition occurs, because the viscosity of the materials gradually decreases by
 539 several orders of magnitude due to an increase in temperature with depth (Eq. 8). The
 540 exact location of the transition is governed by the laboratory-derived viscous paramet-
 541 ers in the wet quartzite flow law (Table 2). In the ductile regime, the stress variabil-
 542 ity between events is small, but all stress fields show the same highly heterogeneous be-
 543 haviour. These stress heterogeneities are mainly caused by the close proximity and in-
 544 termittent presence of mixed pockets of basalt, gabbro and mantle. These lithologies have
 545 different viscous flow law parameters and thus have a different viscosity for the same tem-
 546 perature and pressure conditions. This leads to distinct differences in stress build-up and
 547 relaxation, which causes a highly heterogeneous stress state.

548 Fig. 7 focuses on the stress and strength conditions for the coupled event to anal-
 549 yse where failure is occurring in each of the models. According to their failure criterion,
 550 the SC model compares the initial second invariant of the stress tensor σ'_{II} with the strength
 551 $\sigma_{\text{yield}}^{\text{sc}}$ of the rock, whereas the DR model compares the initial shear stress τ to the fault
 552 yield strength $\sigma_{\text{yield}}^{\text{dr}}$. In the following sections, the term “stress” is generally used to re-
 553 fer to both σ'_{II} and τ , and “strength” is used to refer to $\sigma_{\text{yield}}^{\text{sc}}$ and $\sigma_{\text{yield}}^{\text{dr}}$.

554 The values for the second invariant of the deviatoric stress $\sigma'_{II} = \sqrt{\sigma_{xx}^2 + \sigma_{xz}^2}$ in
 555 the SC model range from 1.4 MPa to 37.8 MPa. In the shallow part of the fault, where
 556 the fault is embedded in the sediments of the accretionary wedge, the stress and strength
 557 are close, which reflects the constant closeness to failure of creeping patches during the

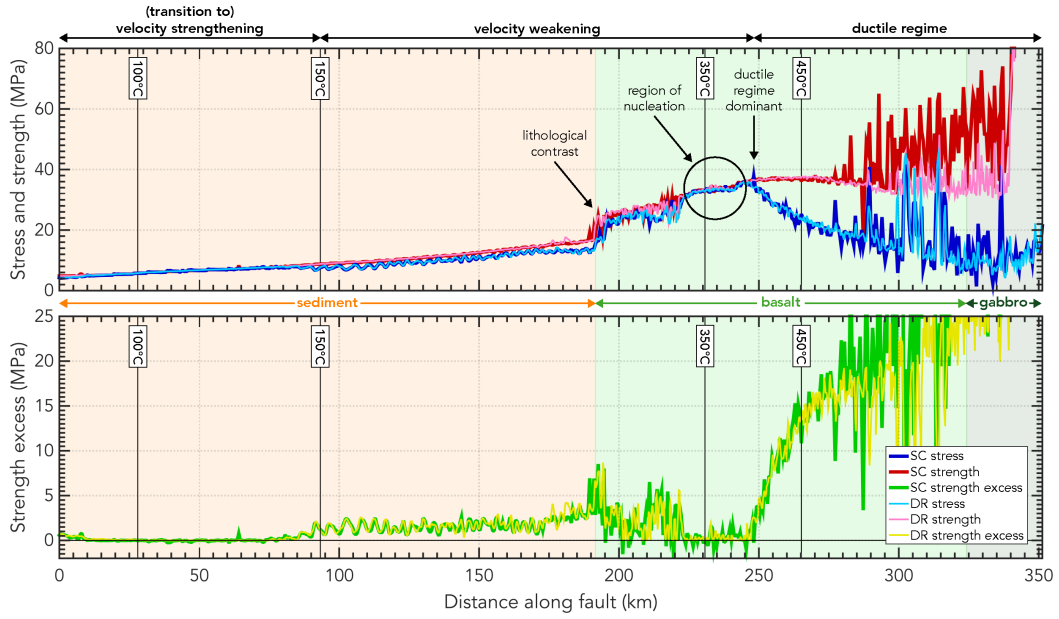


Figure 7. Failure analysis of the SC and DR model on the fault. Second invariant of the deviatoric stress tensor σ'_{II} , strength $\sigma_{\text{yield}}^{\text{sc}}$, and strength excess $\sigma_{\text{yield}}^{\text{sc}} - \sigma'_{II}$ for the SC model (bold lines); and initial shear stress τ , fault yield strength $\sigma_{\text{yield}}^{\text{dr}}$, and strength excess $\sigma_{\text{yield}}^{\text{dr}} - \tau$ for the DR model (thin lines) in the fault coordinate system. Frictional regimes dependent on temperature are indicated with corresponding isotherms (solid black lines). Background colours represent the material through which the fault is going.

558 interseismic period. The proximity of sediments and basalt in the subduction channel
 559 results in a material change on the fault with a corresponding stress and strength change,
 560 as these two materials have different elastic moduli, friction and cohesion values (Fig. 4
 561 and Table 2). The stress and strength variability between 192 and 223 km along the fault
 562 is large, because there are isolated patches of subducted sediments in the basalt close
 563 to the fault that locally affect the stress and strength on the fault. The nucleation re-
 564 gion is located in the basaltic region near the down-dip limit of the seismogenic zone.
 565 For the chosen coupling time step from the SC model, stress reaches the strength of the
 566 basalt at the nucleation region ~ 225 – 245 km along the fault. The peak stress in the
 567 basalt reaches 37.8 MPa. The stresses drop when the viscous behaviour becomes dom-
 568 inant at 248 km along the fault. The material change from basalt to gabbro is not ac-
 569 companied by a distinct change in stress or strength. This is because the frictional prop-
 570 erties no longer dictate the stress and strength of the rock in the ductile regime. The os-
 571 cillations of the stress and strength in the ductile regime are caused by material hetero-
 572 geneity. Smaller oscillations, as observed in the sediment and basalt are due to mapping
 573 the SC properties on the discrete DR fault with the nearest neighbour interpolation.

574 **5.2 Geodynamic seismic cycle slip event**

575 Fig. 8 shows the on-fault evolution of slip rate during both the SC and DR events
 576 through space and time. Important features are indicated by numbers, which are dis-
 577 cussed in this and the following section.

578 The slip rate of the SC model in Fig. 8a shows the initial nucleation phase indi-
 579 cated by (1) during which slip rates are still low $V < 1.0 \cdot 10^{-9}$ m/s. After ~ 50 years,
 580 the rupture starts propagating mainly updip until it is stalled when entering the velocity-
 581 strengthening region (2) and the ductile regime (3), respectively. The highest slip rates
 582 of $5.7 \cdot 10^{-9}$ m/s are reached in the sediments. There is continuous creeping on the fault
 583 in the ductile regime with slip rates of $\sim 3 \cdot 10^{-10}$ m/s. The SC event lasts for 180 years
 584 due to the 5 year time step and the low characteristic velocity in the slip rate-dependent
 585 friction formulation. The low slip rate during the rupture on the order of 10^{-9} m/s is
 586 a direct result of this. Note that due to the evaluation of this event with the nearest neigh-
 587 bour interpolation at the fault geometry approximation adopted for the DR model, we
 588 see visual artefacts in the form of stripes (4) in Figs. 8a,b. Similar artefacts are intro-

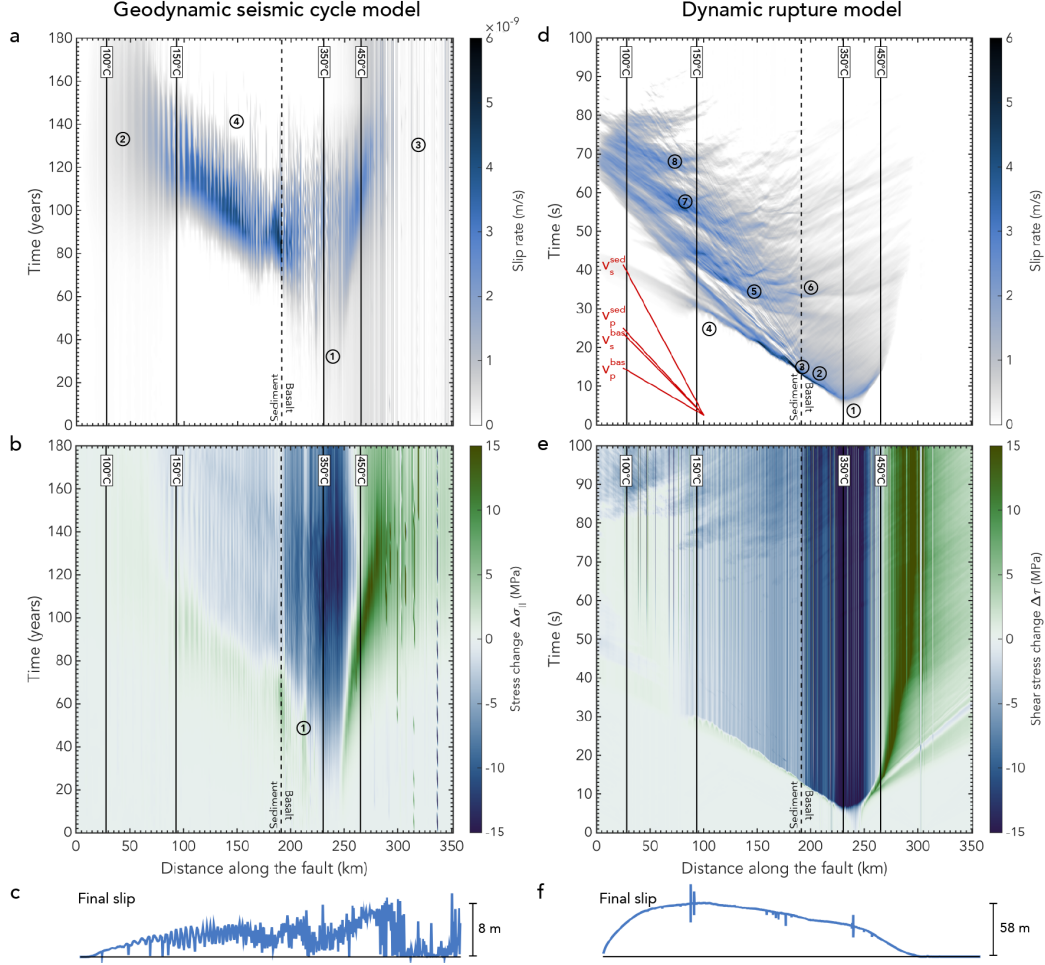


Figure 8. Temporal slip rate evolution with time (a,d), temporal stress change evolution (b,e), and final accumulated slip (c,f) along the fault for the same rupture in the SC model (left column) and the DR model (right column). Solid lines indicate the isotherms that define the frictional regimes; dotted line indicates material change. The P- and S-wave velocities v_p and v_s for both the basalt (_{bas}) and sediment (_{sed}) are indicated in red. Numbers are discussed in the text. We take $t = 0$ years in the SC model for the time step at which we transfer the stresses. The oscillating behaviour visible in the SC final slip distribution stems from the visualisation of the interpolation of the continuous SC model on the discrete DR fault. Low slip rates and high stress drop near the nucleation region likely show the approximated fault does not capture the main slip patch there. Peak slip is indicated.

589 duced in the DR coupling by the interpolation of the coarse SC model resolution vari-
 590 ables onto the high resolution DR fault.

591 The corresponding stress change along the fault with respect to the initial stress
 592 of the event over time always shows a stress increase (1) ahead of the rupture front due
 593 to the conservation of momentum (Fig. 8b). We observe a maximum stress drop of 15 MPa
 594 in the nucleation region. The stress drop is material dependent, as the stress drop in the
 595 basalt is 9.4 MPa on average, whereas the average stress drop of the sediments is 2.8 MPa.
 596 We find an average stress drop of 5.6 MPa between the 150°C and 450° isotherms. When
 597 the frictional regime transitions from velocity-weakening to velocity-strengthening at the
 598 updip limit of the seismogenic zone, the stress drop becomes very small.

599 The final slip distribution in Fig. 8c shows high slip with a maximum of 8.3 m in
 600 the deeper part of the seismogenic zone, which decreases towards the trench and the duc-
 601 tile regime. Note that slip below the 450° isotherm is largely the result of continuous,
 602 ductile creep.

603 **5.3 Coupled dynamic rupture event**

604 The initial conditions imported from the SC model result in the spontaneous nu-
 605 cleation of an earthquake within the DR model (Fig. 8d, (1)) without using any artifi-
 606 cial nucleation procedures. The nucleation phase before the spontaneous rupture prop-
 607 agation lasts for ~ 6.5 s and results in a large nucleation patch of ~ 27 km between
 608 $x = 222$ km and $x = 249$ km along the fault. In the DR model, failure also occurs im-
 609 mediately between $x = 10$ km and $x = 75$ km, which are the regions where shallow
 610 interseismic creep is seen in the SC model (Fig. 7). This instantaneous failure does not
 611 lead to the nucleation of a large earthquake, but does emit seismic waves. The associ-
 612 ated stress drops are on the order of ~ 0.1 MPa and thus low compared to the stress drop
 613 of the main rupture. The friction increases slightly in the velocity-strengthening sedi-
 614 ments from its static value of 0.0176 to a dynamic value of 0.0177. Slip rates of 0.08 m/s
 615 are reached locally and accumulate 0.04 m of slip. We do not observe pronounced inter-
 616 action of the instantaneously emitted waves with the down-dip nucleating spontaneous
 617 rupture event. Importantly, the DR instantaneous failure of the SC creeping sections leaves
 618 behind a heterogeneous initial stress configuration close to, but not at, failure (S param-
 619 eter ~ 0.01 after the initial stress drops, see Appendix C). These fault sections are read-

620 ily re-activated by the main rupture later on. Another considerable instantaneous stress
 621 drop of ~ 4.0 MPa occurs between $x = 219$ km and $x = 222$ km along the fault. Al-
 622 though this stress drop is also low compared to the stress drop of the main rupture, the
 623 downwards travelling emitted seismic waves do interact with the upward travelling main
 624 rupture front. However, the associated mean slip rate of 0.0022 m/s and slip of 0.05 m
 625 are low compared to the main rupture.

626 After the nucleation phase, the rupture mainly propagates updip. There is spon-
 627 taneous rupture arrest below the downdip limit of the seismogenic zone 290 – 300 km along
 628 the fault. In the basalt, supershear rupture speeds of ~ 6100 m/s ($v_p = 6164$ m/s; $v_s =$
 629 3559 m/s) are reached at the onset of rupture. These speeds are promoted by a low S
 630 parameter of 0 – 0.5 (e.g., Gabriel et al., 2012), which is defined as the ratio between ini-
 631 tial strength excess and nominal stress drop (Das and Aki (1977b); Appendix C). Closely
 632 spaced secondary non-supershear rupture fronts (2) follow this main supershear rupture
 633 front. The rupture velocities change when the rupture enters the lower seismic velocity
 634 sediments (3). The main rupture front propagates updip at supershear velocities of \sim
 635 3340 m/s ($v_p = 3350$ m/s; $v_s = 1934$ m/s), and the second rupture fronts travel at
 636 speeds of ~ 1750 m/s in the sediment close to its Rayleigh speed. The change in ma-
 637 terial, and hence seismic velocities, also results in an impedance contrast, which causes
 638 the reactivation of fault slip due to reflected seismic waves from the sediment–basalt tran-
 639 sition (3). Rupture propagation in the sediments in the shallow part of the megathrust
 640 features small scale failure preceding the main rupture front arrival (4). These phases
 641 have slip rates of ~ 0.5 m/s and their rupture speeds are low with 1700 m/s. Their oc-
 642 currence is promoted by (i) a very low strength excess of 1.0 MPa; and (ii) on-fault, dy-
 643 namic stress accumulation preceding the main rupture front. These localised precursory
 644 phases do not merge into a combined rupture front but are overtaken by the faster main
 645 rupture.

646 The rupture is predominantly crack-like, although pulse-like behaviour is observed
 647 in the sediments. Crack-like rupture behaviour is characterised by continuous slip on the
 648 fault after arrival of the rupture front (Kostrov, 1964). During a pulse-like rupture, slip
 649 on the fault only occurs for a relatively small amount of time after the arrival of the rup-
 650 ture front compared to the entire duration of the rupture (Brune, 1970).

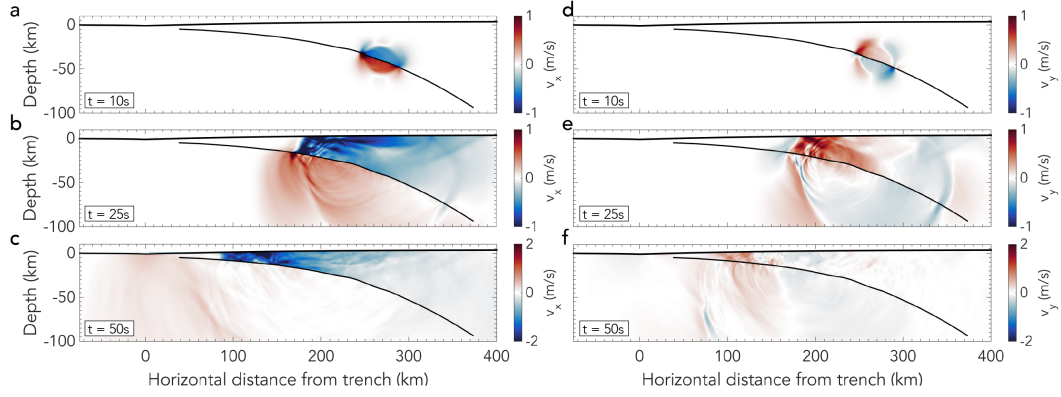


Figure 9. Horizontal (a,b,c) and vertical (d,e,f) velocity in the DR coupling model of Sec. 5.3 at $t = 10$ s, $t = 25$ s and $t = 50$ s. Fault is indicated in black.

651 Surface reflections at (5) provide additional energy to the rupture, which results
 652 in the breaking of the shallow megathrust. This is in line with similar behaviour found
 653 by Kozdon and Dunham (2013) for dynamic rupture models of the 2011 Tōhoku-Oki earth-
 654 quake. Waves are also reflected at the material contrast between sediments and basalt
 655 at (6). Later surface reflections at (7) and (8) reactivate the downdip part of the megath-
 656 rust. The highest slip rate values of 10.9 m/s are reached as the rupture tip reaches the
 657 sediment-basalt transition.

658 The stress drop in Fig. 8e, calculated as the stress change with respect to the ini-
 659 tial stress, is material dependent, with large stress drops of 14 MPa in the basalt and
 660 5.3 MPa in the sediments. The average stress drop between the 150°C and 450° isotherms
 661 is 9.3 MPa. Initially, there is little stress drop in the velocity-strengthening region at the
 662 updip limit of the seismogenic zone. However, after ~ 70 s, the stresses drop in the sed-
 663 iments, even though fault slip has stopped. This could be due to (i) dynamic on-fault
 664 stress transfers caused by healing fronts of the rupture pulses (e.g., Nielsen & Madariaga,
 665 2003; Gabriel et al., 2012), or (ii) dynamically triggered reactivation of the fault by the
 666 seismic waves (e.g., Belardinelli et al., 2003).

667 The corresponding final slip distribution in Fig. 8f shows that the maximum slip
 668 of 57.9 m (disregarding the unphysical isolated peaks) occurs in the sediments, at the
 669 frictional updip limit of the seismogenic zone. Slip tapers off towards the trench and the
 670 downdip limit of the seismogenic zone.

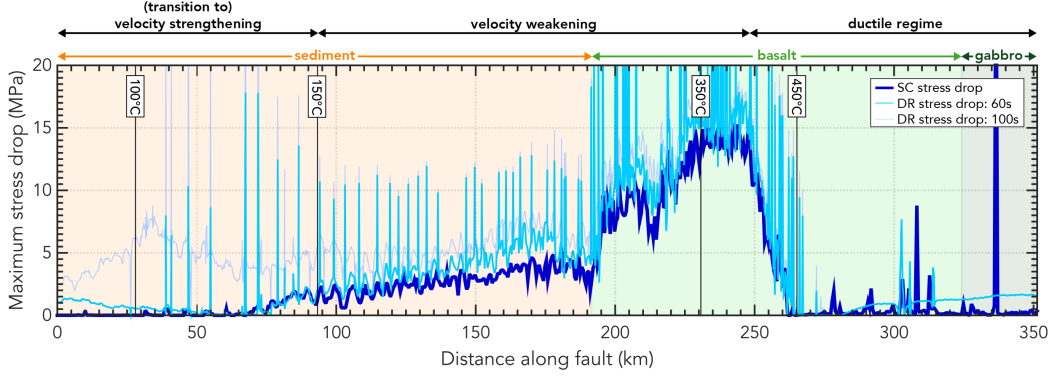


Figure 10. Maximum stress drop in the SC model and DR model (after the first 60 s and at the end of the event at 100 s) along the fault. The peaks of high stress drop in the DR model responsible for the stripes in Fig. 8e are directly related to the input from the SC model. Since the resolution in the DR model is higher, isolated fault points get affected by the interpolation of the coarser model input from the SC model. Frictional regimes dependent on temperature are indicated with corresponding isotherms (solid black lines). Background colours represent the material through which the fault is going.

671 Fig. 9 visualises the wave field at several time steps. At 10 s the rupture just nu-
 672 cleates completely (also see Fig. 8d) and the wave field looks relatively simple. After 25 s,
 673 complex interactions between the free surface and the emitted waves are visible. Most
 674 notably, a large reflected wave is travelling towards the fault. After 50 s most of the waves
 675 are trapped in the accretionary wedge. This results in continuous reactivation of the fault
 676 slip which highly increases the slip in the shallow part of the fault.

677 5.4 Comparison of events in the seismic cycle and dynamic rupture mod- 678 els

679 Both events nucleate in the same location, which demonstrates the successful cou-
 680 pling of fault stress and strength conditions (Fig. 7 and 8). These coupled initial con-
 681 ditions then affect the full dynamic rupture behaviour. Most notably, they cause spon-
 682 taneous rupture arrest at depth ($z = 65$ km) in the DR model due to the increase of
 683 strength excess when the deformation mechanism changes from brittle to ductile in the
 684 SC model (Sec. 5.1).

685 Using the stress and strength of the SC model as input for the DR model results
686 in material dependent stress drop in the DR model. Prior to slip reactivation due to wave
687 reflections, the stress drop values and distribution of the DR event are similar to those
688 of the SC event (Fig. 10). In the nucleation region the stress drop is on the order of \sim
689 14 MPa. After 60 s of rupture, the stress drop in the DR model increases due to reac-
690 tivation of rupture due to the reflected seismic waves that are not present in the SC model.
691 Therefore, the DR model shows higher final stress drops in the sediments than in the SC
692 model. The similarity of the stress drops between the models before the reactivation of
693 fault slip in the DR model demonstrates the successful coupling of the two codes even
694 though their friction behaviour is described by different laws (secs. 2.3 and 3.2).

695 The slip distribution and absolute values of the SC and DR model are different,
696 since the DR model additionally resolves the emitted seismic waves that reactivate fault
697 slip and uses a lower Poisson's ratio. The contributions of the reflected waves and Pois-
698 son's ratio on fault slip are explored in Secs. 5.5 and 6.1.1.

699 In summary, the SC and DR rupture are qualitatively comparable in terms of rup-
700 ture nucleation, propagation, and arrest. They are also quantitatively comparable in terms
701 of stress drop. However, the amount of slip is significantly larger in the DR model.

702 **5.5 The role of complex lithological structures**

703 A common simplification in many dynamic rupture studies is the use of homoge-
704 neous material and friction parameters (e.g., Ma, 2012; Huang et al., 2013). However,
705 in models that include material contrasts, particularly close to the fault, it has been shown
706 that lithological structures affect the rupture (e.g., Huang et al., 2014; Pelties et al., 2015;
707 Lotto et al., 2017). Lithological structures refer to large scale rock or material variations
708 with different properties. Waves reflecting of lithological contrasts are governed by the
709 impedance contrast between rock types. Seismic impedance Z is defined as seismic wave
710 velocity times density ($Z = v \cdot \rho$, see Tables 2 and 3 for values). Large impedance con-
711 trasts favour wave reflection, whereas no or small impedance contrasts favour wave trans-
712 mission. The reflected waves can impact the fault again which affects the on-fault stress
713 field and thereby the rupture dynamics. For example, the resulting on-fault stress changes
714 can lead to the (re-)activation of fault slip and alter the rupture speed (Sec. 5.3; Koz-
715 don & Dunham, 2013; Huang et al., 2014; Pelties et al., 2015).

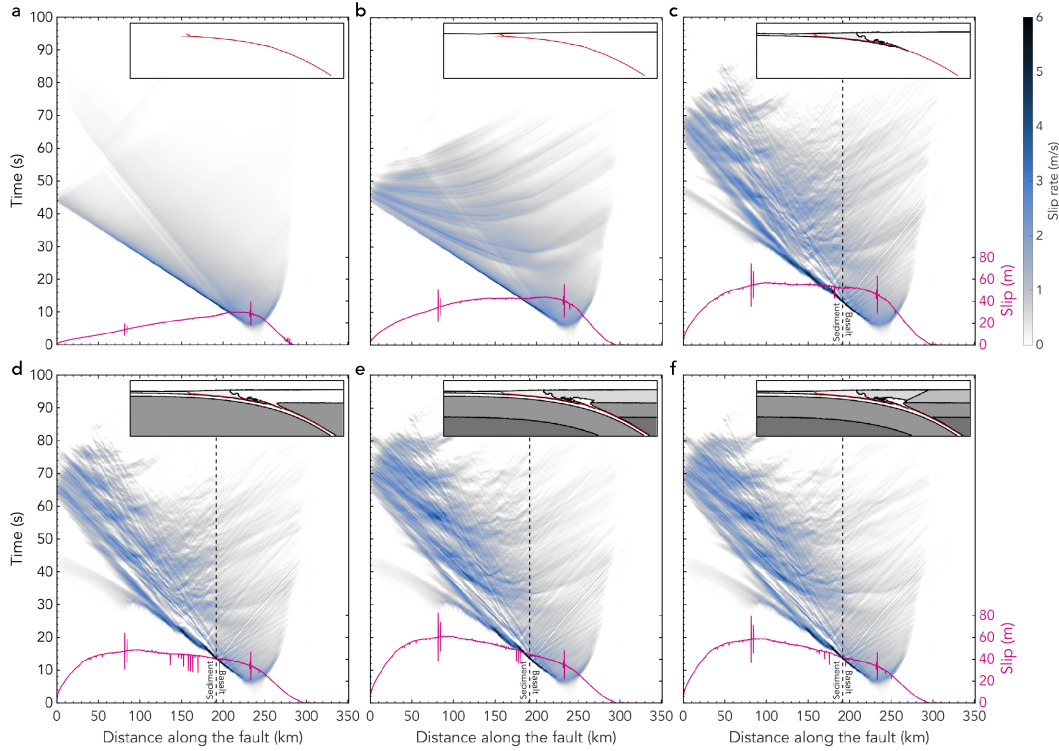


Figure 11. Slip rate evolution of a megathrust rupture for (a) a homogeneous model with basaltic composition and an extended top boundary to exclude any interactions of the seismic waves with the free surface; (b) a homogeneous model with basaltic composition including the free surface as the top boundary condition; (c) the model of Fig. 11b with the addition of incoming sediments; (d) the model of Fig. 11c with the addition of lithospheric mantle; (e) the model of Fig. 11d with the addition of asthenospheric mantle and accretionary wedge sediments; (f) the model of Fig. 11e with the addition of continental crust. Insets show the lithological structure (grey scale colours) and impedance contrasts (black) (Fig. 4a). Dotted line indicates material change between basalt and sediments. Pink lines show the final slip distribution on the fault.

716 The SC model provides a complex geometry with temperature-dependent elastic
 717 properties for the DR model, which results from millions of years of thermo-mechanically
 718 coupled subduction. We systematically increase the complexity of our models from ho-
 719 mogeneous material parameters up to the complex temperature-dependent coupling model
 720 presented in Sec. 5.3 to analyse the effect of each lithological entity on the rupture dy-
 721 namics. Fig. 11 shows the slip rate evolution for six models with an increasingly com-
 722 plex lithological structure as depicted by the insets. The corresponding final slip distri-
 723 bution is also indicated in each panel.

724 In the simplest model, we consider a homogeneous medium with basaltic material
 725 properties. We remove the free surface by extending the top boundary and placing ab-
 726 sorbing boundary conditions on it (Fig. 11a). This effectively removes any reflections of
 727 the seismic waves from impedance contrasts or the free surface. The ensuing rupture is
 728 a supershear crack followed by a subshear crack. The crack-like nature of the rupture
 729 leads to a maximum slip accumulation in the nucleation region, which tapers towards
 730 the surface and brittle-ductile transition. The maximum slip that is reached in this ho-
 731 mogeneous model is 29.5 m, which is twice as low as the maximum slip in the fully com-
 732 plex model of Sec. 5.3. The slip distribution is similar to the one from the SC model (Fig. 8c),
 733 which does not account for seismic waves. In the shallowest 100 km of the fault, the max-
 734 imum slip is 16.7 m. This is more than 3 times less than in the model from Sec. 5.3, where
 735 the peak slip of 57.9 m is reached in the shallowest 100 km of the fault.

736 When a free surface is added to the model in Fig. 11a, the seismic waves reflect off
 737 of it. When they reach the fault, these reflections lower the normal stress on the fault.
 738 This results in an increase in fault slip rate and associated reactivation of fault slip (Fig. 11b).
 739 Because of the prolonged slip reactivation, the rupture duration and the total amount
 740 of slip on the fault increases. The slip is particularly increased in the shallow part of the
 741 fault where the reactivation of fault slip due to reflected waves is most pronounced.

742 When the incoming sediments of the accretionary wedge are added to the model
 743 in Fig. 11c, they introduce a low-velocity region, as the seismic velocities of the sediments
 744 are lower than that of the surrounding basalt. The impedance contrast between the sed-
 745 iments ($Z = 8.7 \cdot 10^6 \text{ kg / s m}^2$) and basalt ($Z = 18.5 \cdot 10^6 \text{ kg / s m}^2$) is large. This
 746 addition to the model results in a change of the rupture behaviour from predominantly
 747 crack-like to pulse-like. Pulse-like behaviour of the rupture is promoted by reflections

748 that induce a stress change favourable for fault slip. Whether a reflection induces a posi-
749 tive or negative stress change depends on their polarity. When a stress change occurs
750 that is unfavourable for slip, the slip on the fault stops which results in pulse-like behaviour
751 (Huang et al., 2014).

752 The large impedance contrast also causes a large portion of the seismic waves to
753 get trapped in the incoming sediments (also see Fig. 9). This results in a complex slip
754 reactivation pattern on the fault that increases the accumulated slip on the fault in the
755 sediments. The isolated patches of subducted sediment in the basalt in the vicinity of
756 the sediment-basalt transition also cause a lot of wave reflections, refractions and inter-
757 actions. This leads to pronounced rupture fronts in the basalt. Small nucleations in the
758 sediments are facilitated by the low strength excess in the sediments.

759 The addition of lithospheric mantle changes the shape of the slip distribution (Fig. 11d).
760 Waves reflecting from the free surface impact the deeper part of the fault less heavily
761 than before, because the impedance contrast between the basaltic top layer and the litho-
762 spheric mantle is smaller and leads to less reflections. The lower wave amplitudes result
763 in less fault slip reactivation in the basalt than in Fig. 11c. Therefore, the accumulated
764 slip in the basaltic part of the fault is lower. The addition of lithospheric mantle also ef-
765 fectively transforms the deeper part of the fault that is going through the basalt into a
766 low velocity region. However, the impedance contrast between the lithospheric mantle
767 and the basalt is more than twice as low as the impedance contrast between the basalt
768 and sediments. The effect of this lower velocity region is therefore not as pronounced as
769 in Fig. 11c and we do not see pulse-like rupture behaviour in the basalt. The pulse-like
770 behaviour of the rupture in the sediments is enhanced, even though the lithospheric man-
771 tle and the incoming sediments are not directly adjacent.

772 Adding asthenospheric mantle material to the model does not change any of the
773 on-fault properties or the rupture. This is due to the low impedance contrast between
774 lithospheric and asthenospheric mantle. Combined with the large distance between this
775 impedance contrast and the fault, the on-fault effect of this material contrast is negli-
776 gible on the rupture dynamics.

777 The addition of the accretionary wedge sediments adds a larger impedance contrast
778 at the base of the wedge with the basalt (Fig. 11e). There is also an impedance contrast

779 between the accretionary and incoming sediments, which causes additional reflections.
780 This results in more reactivation of slip within the sediments.

781 The continental crust of the overriding plate is the last component of the SC sub-
782 duction zone setup that we add to the model (Fig. 11f). Its addition results in less slip
783 reactivation on the fault. Hence, the accumulated slip in Fig. 11f (maximum slip disre-
784 garding the unphysical slip peaks at isolated fault points is 59.2 m) is less than in Fig. 11e
785 (maximum slip disregarding the unphysical slip peaks at isolated fault points is 61.4 m).

786 The models in Fig. 11 all assume constant material properties per rock type. How-
787 ever, one of the advantages of the SC model is that it provides temperature- and pressure-
788 dependent densities. Comparing the model of Fig. 11f to Fig. 8d shows that the slip pulses
789 on the fault are less pronounced when a temperature-dependent density is considered.
790 This is due to less energetic reflections from decreased impedance contrasts related to
791 the gradual increase of density and their related seismic velocities. Hence, the use of temperature-
792 dependent properties leads to $\sim 1\text{--}2$ m less slip on the fault.

793 In summary, these results show that material contrasts influence the rupture dy-
794 namics by causing slip reactivation on the fault and influencing the final slip distribu-
795 tion. The model with purely homogeneous material properties significantly underesti-
796 mates the shallow fault slip by a factor 3 and results in a vastly different slip distribu-
797 tion. Using the temperature-dependent material contrasts of the SC model consistent
798 with the fault geometry, stress, and strength, is crucial to resolve the complex wave in-
799 teractions during rupture in a subduction zone which in turn affects the dynamics of the
800 megathrust earthquake.

801 **5.6 The impact of physically consistent stresses on splay fault activa-** 802 **tion**

803 For simplicity, we only considered a rupture along the megathrust in the previous
804 sections. However, the SC model shows high strain rate localisation along a splay fault
805 instead of the shallow megathrust. However, the slip rates are not high enough to reach
806 the threshold that defines a seismic event (Secs. 4.1 and 4.3). Here, we introduce the splay
807 fault to the model by activating its internal frictional boundary condition so that slip
808 on the splay fault is theoretically possible. This allows us to analyse if the splay fault
809 is activated in the DR model when seismic waves are taken into account.

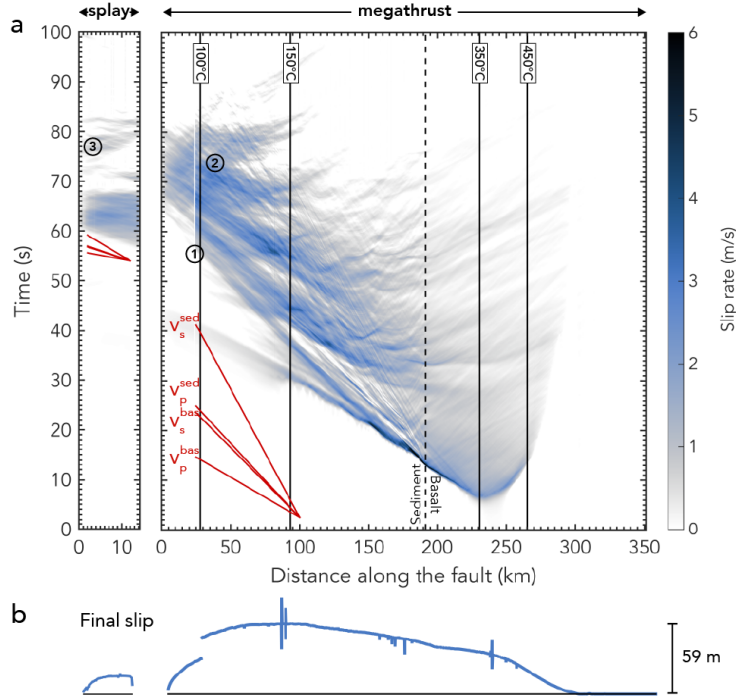


Figure 12. Slip rate evolution with time (a) and final accumulated slip (b) along the fault for both the splay fault (left column, note the horizontal exaggeration with respect to the megathrust fault x -axis) and the megathrust (right column). The splay fault connects to the megathrust at $x = 24.5$ km along the megathrust fault. Solid lines indicate the isotherms that define the frictional regimes; dashed line indicates material change. The P- and S-wave velocities v_p and v_s for both the basalt (^{bas}) and sediment (^{sed}) are indicated in red in both the splay and megathrust panels. Numbers are discussed in the text. The branching point on the megathrust and the two adjacent points to the left of the branching point are not plotted, as they show an unphysical numerical instability. Peak slip is indicated.

810 The resulting rupture evolution in terms of its slip rate and the final slip distribu-
 811 tion of both the megathrust and splay fault are shown in Fig. 12. The splay fault in the
 812 DR model is activated at 56 s (Fig. 12a). Comparison with the reference model in Fig. 8
 813 shows that both ruptures have a similar evolution. When the splay fault is activated at
 814 (1), the rupture chooses the splay fault over the megathrust and it continues at much
 815 lower slip rates on the megathrust than in the reference model ($\sim 56\text{--}68$ s). This is also
 816 clearly illustrated in the final slip profile (Fig. 12b), as the final slip on the shallow megath-
 817 rust is sharply reduced at the location of the splay fault compared to the reference model
 818 (Fig. 8f). Instead, we see 20 m of slip on the splay fault. When the splay fault is aban-
 819 doned at approximately 68 s, the rupture in the shallow part of the megathrust looks
 820 very similar to the reference model results with the exception that small reflections from
 821 the splay fault on the megathrust are visible in the splay model (2). The last surface re-
 822 flection at ~ 74 s reactivates the splay fault (3). Combining the slip on the splay fault
 823 with that of the shallowest megathrust fault, we see that the same amount of slip is ac-
 824 cumulated in total as on the megathrust in the DR model of Sec. 5.3.

825 In summary, our model shows that the splay fault is indeed activated in the DR
 826 model, depicting maximum slip rates of 2.4 m/s and a maximum slip of 20 m, which is
 827 much higher than what is observed in the corresponding SC model. Therefore, we need
 828 to account for additional fault complexities such as faults splaying off from the megath-
 829 rust interface to fully assess the seismic and tsunami hazard of subduction zone earth-
 830 quakes.

831 6 Discussion

832 By coupling a geodynamic seismic cycle model to a dynamic rupture model, we suc-
 833 cessfully modelled the geodynamic evolution of a subduction zone down to a single dy-
 834 namic earthquake rupture of the megathrust. Broad rupture characteristics, such as the
 835 rupture nucleation, propagation, and arrest, of the SC event and its corresponding DR
 836 counterpart are qualitatively comparable. The seismic waves and a complicated subsur-
 837 face structure affect the slip distribution on the fault, rupture style and duration. A ho-
 838 mogeneous model significantly underestimates shallow fault slip, which has implications
 839 for tsunami hazard assessment. With our coupling method, we can also take into account
 840 complex fault geometries including splay faults. The complex resulting dynamic rupture

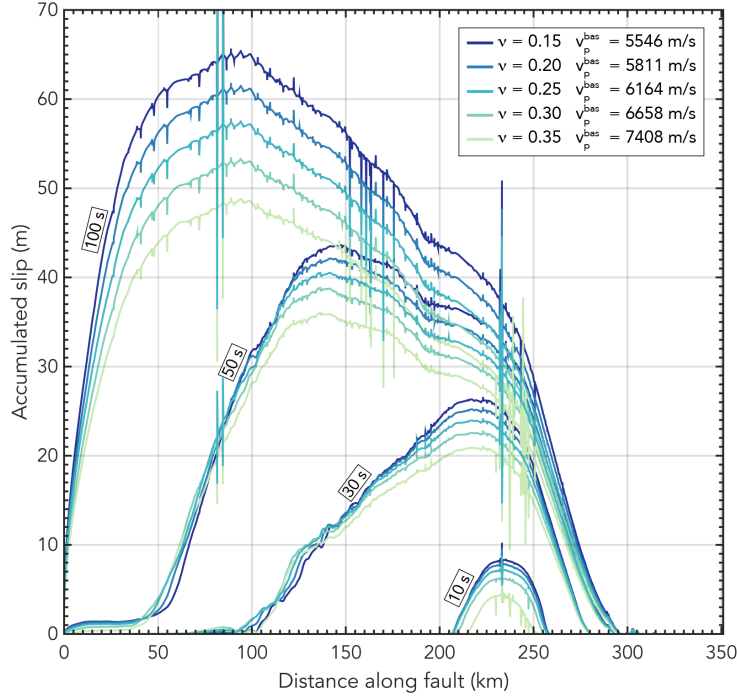


Figure 13. Accumulated slip along the fault plotted after 10 s, 30 s, 50 s and 100 s for five models where the first Lamé parameter was calculated using different Poisson’s ratios. The corresponding change in P-wave velocity is indicated for the basalt. Note that the model with $\nu = 0.25$ is the model described in Sec. 5.3.

841 highlights the need for taking all scales into account when assessing the seismic and tsunami-
 842 genic hazard of megathrust earthquakes.

843 In the following, we discuss our two most important coupling assumptions neces-
 844 sary to reconcile the SC and DR method. Namely, our choice of the Poisson’s ratio, and
 845 the approximation of the SC model’s rate-dependent friction by linear-slip weakening
 846 in the DR model. Lastly, we discuss limitations and future developments.

847 **6.1 Effect of coupling choices**

848 **6.1.1 Poisson’s ratio**

849 To calculate the first Lamé parameter in the DR model from the incompressible
 850 SC model rock properties, we need to assume a Poisson’s ratio. Computational seismol-
 851 ogy often uses Poisson solids as a simplification, where $\nu = 0.25$ and therefore $\lambda_1 =$
 852 G (e.g., Stein & Wysession, 2009; Kozdon & Dunham, 2013). In line with this, we cal-

853 culated λ_1 with $\nu = 0.25$ for our coupled event in Sec. 5. However, laboratory exper-
 854 iments indicate that there is a large variation in the Poisson’s ratio of intact rocks, e.g.,
 855 the Poisson’s ratio of basalt ranges from 0.1–0.35 (Gercek, 2007).

856 An increase in Poisson’s ratio results in an increase of the P -wave velocity v_p , and
 857 therefore increases the difference between the P - and S -wave velocities according to

$$v_p = v_s \sqrt{\frac{2\nu}{1 - 2\nu} + 2}. \quad (21)$$

858 To assess this effect on our results, we run several models with different Poisson’s
 859 ratios. Models with Poisson’s ratio $\nu > 0.40$ did not result in sustained nucleation and
 860 propagation of the rupture, due to the unrealistically large seismic velocities. For $\nu =$
 861 0.40 several patches in the nucleation region are also already prohibited from rupturing.
 862 Fig. 13 shows the accumulated slip contours for several time steps for models with Pois-
 863 son’s ratio 0.15–0.35. Larger Poisson’s ratios result in less final slip with a maximum
 864 slip of 65.7 m for $\nu = 0.15$ and 49.0 m for $\nu = 0.35$, disregarding the unphysically high
 865 peaks in slip. This is due to a reduction in maximum slip rate and rupture duration. The
 866 latter is caused by both an increase in rupture speed and in nucleation time. The stress
 867 drop is not majorly affected by the Poisson’s ratio.

868 Interestingly, as the slip decreases with increasing Poisson’s ratio, the slip values
 869 of the DR model move towards those of the SC model, which has the highest possible
 870 Poisson’s ratio of 0.5. Using a high Poisson’s ratio for the model described in Fig. 11a,
 871 where seismic wave effects are non-existent would likely result in slip values similar to
 872 those of the SC model. This means that part of the slip difference between the SC and
 873 DR model can be accounted for by the difference in Poisson’s ratio, while a factor of two
 874 to three of slip difference can be accounted for by fault reactivation due to wave reflec-
 875 tions (Sec. 5.5).

876 The parameters affected by the Poisson’s ratio (i.e., the maximum slip, rupture du-
 877 ration, slip rate, nucleation time, and rupture velocity) do not change the first order rup-
 878 ture characteristics, i.e., material dependent stress drop and predominantly updip rup-
 879 ture propagation, which are comparable to its SC rupture equivalent, or the rupture style.

880 **6.1.2 Rate-dependent friction law approximation**

881 In this study, we approximate the rate-dependent friction law of the SC model by
 882 a linear slip weakening friction law in the DR model. It is one of the simplest friction
 883 laws and it is widely used in the dynamic rupture community (e.g., Ma, 2012; Murphy
 884 et al., 2016). However, several other friction laws could have been used. For example,
 885 Olsen-Kettle et al. (2008) discusses the cubic, quintic, and septic slip weakening friction
 886 laws which are found to reduce the amount of slip.

887 Translating the rate-dependent friction formulation of the SC model to the linear
 888 slip weakening formulation of the DR model requires determining D_c . By ensuring both
 889 friction laws have the same strength drop with slip (Secs. 4.4 and Fig. 5), we have a phys-
 890 ical basis for picking a certain D_c value. The resultant D_c varies between 0.7–1.1 m in
 891 the sediments, which is in line with values used in the dynamic rupture community for
 892 similar problems (e.g., Goto et al., 2012; Murphy et al., 2016). The values for D_c in the
 893 basalt are slightly higher and range from 1.0–3.5 m with values from 0.7–3.0 m in the
 894 nucleation region.

895 An alternative way to couple the two friction laws would be to use the character-
 896 istic slip distance corresponding to the accumulated slip at which the lowest friction value
 897 is reached in the SC model (i.e., D_c would be larger in Fig. 5). To test the effect of D_c
 898 on our model results, we run models with a constant D_c along the fault varying from 0.25–
 899 8 m. We find that the nucleation phase takes longer for increasing D_c . This is consis-
 900 tent with work by Bizzarri et al. (2001). With constant $D_c \geq 4$ m, we do not get nu-
 901 cleation at all. Besides this effect on the nucleation phase of the model, increasing D_c
 902 results in a longer rupture duration accompanied by a smaller maximum slip velocity.
 903 Stress drop, maximum slip, and rupture speed are not significantly affected. As the choice
 904 of D_c does not affect the first-order rupture characteristics, we argue that using the D_c
 905 values obtained from equating the strength drop with slip between the two models re-
 906 sults in robust rupture dynamics.

907 **6.2 Limitations & future work**

908 At present, we couple the frictional parameters of the SC model to the discrete fault
 909 in the DR model. However, the SC model provides information on the stress field and
 910 material strength in the entire domain. This information can be used to extend the cur-

911 rent DR model to account for plastic processes around the fault. Plasticity is found to
912 influence the overall rupture dynamics, as well as the seafloor displacements (Ma, 2012),
913 which will crucially affect the tsunamigenic potential of the faults. The DR model pro-
914 vides the ability to account for off-fault plastic deformation during coseismic rupture (Wollherr,
915 Gabriel, & Uphoff, 2018) and ongoing research is concentrated on coupling the off-fault
916 plastic yielding of the SC model to that of the DR model (Wollherr et al., 2017).

917 Another way to incorporate the large scale yielding in the accretionary wedge of
918 the SC model relies on explicitly meshing the spontaneous splay faults of the SC model
919 in the DR model. Besides coupling the on- and off-fault deformation between the SC and
920 DR model in this manner, explicitly meshing the splay faults gives additional insight into
921 the activation of splays in subduction zones and over several seismic cycles. Realistically
922 modelling splay fault activation using the constraints from the SC model can also con-
923 tribute to our understanding of tsunami generation.

924 Currently, the here presented coupling approach is restricted to two dimensions since
925 the SC model is inherently two-dimensional. The extension of this coupling approach
926 to three dimensions is on-going work within the ASCETE (Advanced Simulation of Cou-
927 pled Earthquake and Tsunami Events) framework (Gabriel et al., 2018), where the two-
928 dimensional initial conditions from the SC model are used in the three-dimensional ver-
929 sion of SeisSol.

930 By extending our approach to three dimensions (e.g., Dunham & Bhat, 2008) and
931 accounting for off-fault plasticity (e.g., Gabriel et al., 2013), we expect that the SC ini-
932 tial conditions are less favourable for supershear rupture. The high slip rate values ob-
933 served in the DR models, which are typical for purely elastic dynamic rupture models
934 (Andrews, 2005), may additionally be limited by including off-fault plastic deformation.

935 **7 Conclusions**

936 We couple geodynamic, seismic cycle, and dynamic rupture modelling to resolve
937 a wide range of time scales governing megathrust earthquake rupture. We use a two-dimensional,
938 visco-elasto-plastic, continuum, seismo-thermo-mechanical model to simulate 4 Myrs of
939 subduction dynamics and the subsequent seismic cycle. The long-term SC model geom-
940 etry features a megathrust dipping at 14° on average and a large accretionary wedge due
941 to sediment accretion. We model 70 quasi-periodic slip events in the seismic cycle phase,

942 which mostly nucleate near the spontaneous down-dip limit of the seismogenic zone. The
943 long-term constrained state of stress varies with lithology and reaches a maximum of 37.8 MPa
944 just above the brittle-ductile transition. For the coupling, we use a representative SC
945 slip event with maximum slip at the nucleation region near the down-dip limit of the seis-
946 mogenic zone. The ductile regime is characterised by low stresses due to viscous stress
947 relaxation and is accompanied by distributed ductile creep.

948 We then couple the full complexity of spatially heterogeneous, self-consistent fault
949 stress and strength, material properties, and megathrust geometry at the onset of the
950 SC slip event to a dynamic rupture model. The use of an unstructured tetrahedral mesh
951 allows for a complex megathrust geometry that results from the SC model. The dynamic
952 rupture model resolves spontaneous earthquake rupture jointly with seismic waves in a
953 two-dimensional elastic model of the megathrust interface.

954 The SC and DR events both nucleate and arrest spontaneously at the same loca-
955 tions. The stress drop in both models compares well and is material dependent, with sed-
956 iments exhibiting a stress drop of ~ 3 MPa in contrast to values of up to 10 MPa in basaltic
957 regions.

958 The dynamic rupture propagates primarily updip in a crack-like fashion within the
959 basalt and in a more pulse-like manner within the sediments. Both sections exhibit sus-
960 tained supershear rupture speeds due to a small relative strength throughout the megath-
961 rust.

962 We systematically demonstrate the pronounced effects of complex lithological struc-
963 tures on rupture complexity, slip accumulation and dynamic fault reactivation. Remov-
964 ing all impedance contrasts that reflect waves decreases peak slip by a factor two. The
965 homogeneous model shows a similar slip distribution to the SC model, which also does
966 not account for reflecting seismic waves. The inclusion of an effective low-velocity zone
967 in the form of sediments changes the rupture style from predominantly crack-like to pulse-
968 like. In addition, seismic waves get trapped in the sediment layer which results in con-
969 tinuous reactivation of fault slip, particularly in the shallow part of the fault.

970 Within the presented coupling framework, we are able to include additional fault
971 structures based on strain localisation in the SC model. Adding a splay fault to the dy-

972 namic rupture simulation results in preferred splay activation. Reflected waves also ac-
 973 tivate the megathrust.

974 Subduction zone geometry, lithology, fault stresses and strength, as constrained by
 975 subduction evolution and seismic cycles, crucially affects the first-order features of earth-
 976 quake rupture dynamics. Our study also reveals important dynamic effects not captured
 977 in seismic cycle approaches, such as the effect of seismic wave reflections from the free
 978 surface on shallow slip accumulation in subduction zones. The SC results in terms of stress
 979 magnitude and variability constrained by 4 Myrs of subduction can be used as a guide-
 980 line for setting up dynamic rupture models of subduction zone megathrusts and splay
 981 faults. This study highlights the key relationships between subduction zone processes
 982 and earthquake dynamics across temporal and spatial scales.

983 **Appendix A Initial conditions governing the SC model**

984 To initiate and sustain subduction, we apply a constant velocity of 7.5 cm/year to
 985 the subducting slab (Fig. 1), which is in line with observations for Southern Chile (Lallemand
 986 et al., 2005). Subduction initiation is further accommodated with a weak zone (Fig. 1),
 987 which follows a wet olivine flow law and has very low plastic strength (Table 2; Gerya
 988 & Meilick, 2011). After 3.2 million years, the initial weak zone is artificially removed and
 989 replaced with lithospheric mantle, so that the weaker material does not influence the model
 990 any more when a suitable subduction geometry has been obtained.

991 The initial temperature field is calculated by considering 1) the age of the subduct-
 992 ing slab (40 Ma, Lallemand et al., 2005) according to the half space cooling model (Turcotte
 993 & Schubert, 2002), 2) a linear temperature increase for the first 100 km of the continen-
 994 tal crust from 0°C to 1300°C, and 3) a 0.5°C km⁻¹ temperature gradient in the astheno-
 995 spheric mantle.

996 **Appendix B Boundary conditions of the SC model**

997 We adopt the same boundary conditions as van Dinther, Gerya, Dalguer, Mai, et
 998 al. (2013) with free slip boundary conditions at the sides, which allow material to freely
 999 move tangential to the boundaries, and an open boundary condition at the bottom (Fig. 1).
 1000 To enhance the decoupling of the lithosphere from the boundaries, we use prescribed low
 1001 viscosity regions at the side and bottom boundaries of the model (van Dinther, Gerya,

1002 Dalguer, Mai, et al., 2013). We apply viscosity limits of minimum $1 \cdot 10^{17}$ Pa s and max-
 1003 imum $1 \cdot 10^{25}$ Pa s throughout the model.

1004 Due to the nature of the finite difference method, we do not have a true free sur-
 1005 face in the SC model. Therefore, we use the sticky air method (Cramer et al., 2012),
 1006 which is a widely used proxy for a free surface in finite difference geodynamics. The sticky
 1007 air method consists of a layer of so-called ‘sticky air’ with low viscosity and density at
 1008 the top of the model where the top boundary condition is free slip (Table 2). It allows
 1009 the air-crust interface to behave as a free surface which can accommodate topography
 1010 evolution.

1011 The temperature is set to 0°C at the top of the domain and we impose zero heat
 1012 flux at the sides. At the bottom boundary, we have a constant temperature boundary
 1013 condition.

1014 **Appendix C Relative strength in the DR model**

1015 To estimate the initial closeness to failure of the fault, we can use several differ-
 1016 ent measurements. In the geodynamics community, the strength excess is commonly used,
 1017 which is the difference between the yield strength of the rock and the initial stresses (Fig. 7b).
 1018 In the dynamic rupture community it is more common to calculate the relative strength
 1019 or so-called S parameter. We calculate the relative strength S for the DR model accord-
 1020 ing to the following formula (Das & Aki, 1977a)

$$S = \frac{\tau_s - \tau_0}{\tau_0 - \tau_d} \quad (\text{C1})$$

1021 where $\tau_s = \sigma_{\text{yield}}^{\text{dr}} = C + \mu_s \sigma_n$ is the fault yield strength or initial static strength of
 1022 the material (see Sec. 3.2). $\tau_d = \sigma_{\text{sliding}}^{\text{dr}} = \sigma_n \mu_d$ is the sliding strength of the mate-
 1023 rial, which can also be called the dynamic strength of the material. τ_0 is the initial shear
 1024 stress. Note that the cohesion C does not enter the sliding strength of the fault. This
 1025 is different to the SC model, where the bulk cohesion is always present in the yield cri-
 1026 terion and strength of the material.

1027 Fig. C1 shows that large parts of the fault are initially at failure with $S = 0$. How-
 1028 ever, these regions do not all result in sustained rupture, as discussed in Sec. 5.3. After
 1029 ~ 15 s, the shallow part of the fault is no longer at failure, i.e. $S > 0$, although the

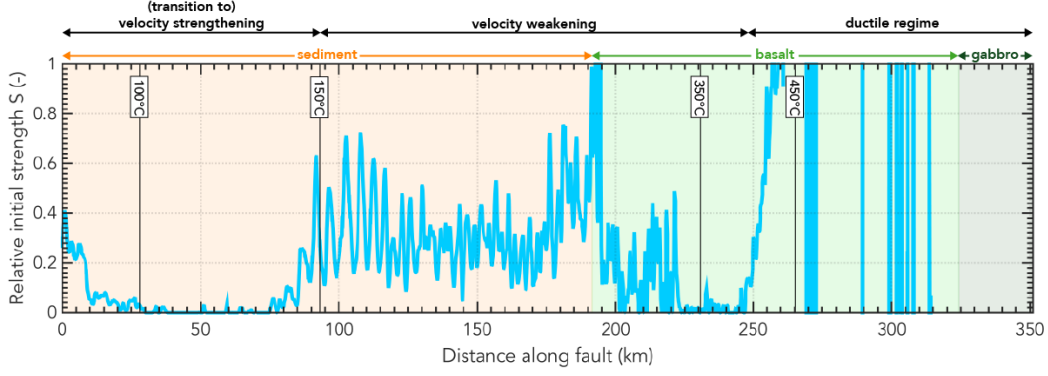


Figure C1. Relative strength S in the DR model along the fault. Frictional regimes dependent on temperature are indicated with corresponding isotherms (solid black lines). Background colours represent the material through which the fault is going.

1030 relative strength is still very low, on the order of 0.05. When the main rupture arrives
 1031 in the shallow part of the fault, it breaks again and S decreases to 0. The relative strength
 1032 in the ductile regime is large ($S \gg 1$, up to 396), which prohibits rupture on that part
 1033 of the fault.

1034 A low relative strength promotes supershear pulses and cracks (e.g., Gabriel et al.,
 1035 2012), which is indeed what occurs for the sustained main rupture in the DR model (Sec. 5.3).

1036 Acknowledgments

1037 Input parameters for the SC model are discussed in Sec. 2.4, Appendix A and Ap-
 1038 pendix B, and Table 2. The DR model setup is discussed in 3.3. The complete input pa-
 1039 rameter file, megathrust and splay fault geometry, and surface geometry can be found
 1040 in the Supporting Information.

1041 We would like to thank Casper Pranger, Marie Bocher, Luca Dal Zilio, Simon Preuss,
 1042 Claudio Petrini, and Robert Herrendörfer for fruitful discussions, insights into the SC
 1043 models, and valuable comments that improved the manuscript. We would also like to
 1044 thank Carsten Uphoff for technical support relating to the meshing of the DR model.

1045 Perceptually-uniform colour maps provided by Fabio Crameri and the cmocean pack-
 1046 age by Kristen Thyng were used in this study to prevent visual distortion of the data.

1047 Computational resources were used on the CSCS clusters Mönch and Piz Daint (project
 1048 no s741), and the ETH cluster Euler. Further computing resources were provided by the
 1049 Institute of Geophysics of LMU Munich (Oeser et al., 2006) and the Leibniz Supercom-
 1050 puting Centre (LRZ, projects no h019z, pr63qo, and pr45fi on SuperMUC).

1051 This work is part of the ASCETE project funded by the Volkswagen Foundation
 1052 (Advanced Simulation of Coupled Earthquake-Tsunami Events, grant no 88479). YvD
 1053 was funded by SNSF grants nos 200021153524 and 200021169880. SW and AAG were
 1054 funded by the European Unions Horizon 2020 research and innovation program (ExaHyPE,
 1055 grant no 671698 and ChEESE, grant no 823844), the German Research Foundation (DFG)
 1056 (projects no KA 2281/4-1, GA 2465/2-1, GA 2465/3-1), BaCaTec (project no A4), and
 1057 KONWIHR - the Bavarian Competence Network for Technical and Scientific High Per-
 1058 formance Computing (project: NewWave).

1059 IvZ developed the coupling method, designed the models, analysed the results, and
 1060 wrote the article. YvD and AAG contributed to the concept development and SW and
 1061 EHM contributed to the development of the coupling method. SW also provided addi-
 1062 tional features to the DR code specifically for the coupling method. All authors discussed
 1063 the results and contributed to the final manuscript.

1064 References

- 1065 Ampuero, J.-P., Vilotte, J.-P., & Sanchez-Sesma, F. (2002). Nucleation of rupture
 1066 under slip dependent friction law: simple models of fault zone. *Journal of Geo-*
 1067 *physical Research: Solid Earth*, *107*(B12).
- 1068 Andrews, D. (1973). A numerical study of tectonic stress release by underground ex-
 1069 plosions. *Bulletin of the Seismological Society of America*, *63*(4), 1375–1391.
- 1070 Andrews, D. (2005). Rupture dynamics with energy loss outside the slip zone. *Jour-*
 1071 *nal of Geophysical Research: Solid Earth*, *110*(B1).
- 1072 Angiboust, S., Wolf, S., Burov, E., Agard, P., & Yamato, P. (2012). Effect of fluid
 1073 circulation on subduction interface tectonic processes: Insights from thermo-
 1074 mechanical numerical modelling. *Earth and Planetary Science Letters*, *357*,
 1075 238–248.
- 1076 Aochi, H., & Fukuyama, E. (2002). Three-dimensional nonplanar simulation of
 1077 the 1992 Landers earthquake. *Journal of Geophysical Research: Solid Earth*,

- 1078 107(B2), ESE-4.
- 1079 Bai, K., & Ampuero, J.-P. (2017). Effect of seismogenic depth and background
1080 stress on physical limits of earthquake rupture across fault step overs. *Journal*
1081 *of Geophysical Research: Solid Earth*, 122(12).
- 1082 Bauer, A., Scheipl, F., Küchenhoff, H., & Gabriel, A.-A. (2017). Modeling spatio-
1083 temporal earthquake dynamics using generalized functional additive regression.
1084 In *Proceedings of the 32nd international workshop on statistical modelling*
1085 (Vol. 2, pp. 146–149).
- 1086 Belardinelli, M., Bizzarri, A., & Cocco, M. (2003). Earthquake triggering by static
1087 and dynamic stress changes. *Journal of Geophysical Research: Solid Earth*,
1088 108(B3).
- 1089 Ben-Zion, Y., & Rice, J. R. (1997). Dynamic simulations of slip on a smooth fault
1090 in an elastic solid. *Journal of Geophysical Research: Solid Earth*, 102(B8),
1091 17771–17784.
- 1092 Billen, M. I. (2008). Modeling the dynamics of subducting slabs. *Annual Review of*
1093 *Earth and Planetary Sciences*, 36, 325–356.
- 1094 Billen, M. I., Gurnis, M., & Simons, M. (2003). Multiscale dynamics of the Tonga-
1095 Kermadec subduction zone. *Geophysical Journal International*, 153(2), 359–
1096 388.
- 1097 Bizzarri, A. (2010). How to promote earthquake ruptures: Different nucleation
1098 strategies in a dynamic model with slip-weakening friction. *Bulletin of the*
1099 *Seismological Society of America*, 100(3), 923–940.
- 1100 Bizzarri, A., Cocco, M., Andrews, D., & Boschi, E. (2001). Solving the dynamic rup-
1101 ture problem with different numerical approaches and constitutive laws. *Geo-*
1102 *physical Journal International*, 144(3), 656–678.
- 1103 Blanpied, M. L., Lockner, D. A., & Byerlee, J. D. (1995). Frictional slip of gran-
1104 ite at hydrothermal conditions. *Journal of Geophysical Research: Solid Earth*,
1105 100(B7), 13045–13064.
- 1106 Bormann, P., Engdahl, B., & Kind, R. (2012). Seismic wave propagation and earth
1107 models. In P. Bormann (Ed.), *New Manual of Seismological Observatory Prac-*
1108 *tice 2 (NMSOP2)* (p. 1 - 105). Potsdam : Deutsches GeoForschungsZentrum
1109 GFZ.
- 1110 Brune, J. N. (1970). Tectonic stress and the spectra of seismic shear waves from

- 1111 earthquakes. *Journal of geophysical research*, 75(26), 4997–5009.
- 1112 Buitter, S. J., Schreurs, G., Albertz, M., Gerya, T. V., Kaus, B., Landry, W., . . . oth-
 1113 ers (2016). Benchmarking numerical models of brittle thrust wedges. *Journal*
 1114 *of structural geology*, 92, 140–177.
- 1115 Chang, C., McNeill, L. C., Moore, J. C., Lin, W., Conin, M., & Yamada, Y. (2010).
 1116 In situ stress state in the Nankai accretionary wedge estimated from borehole
 1117 wall failures. *Geochemistry, Geophysics, Geosystems*, 11(12).
- 1118 Chester, F., & Higgs, N. (1992). Multimechanism friction constitutive model for
 1119 ultrafine quartz gouge at hypocentral conditions. *Journal of Geophysical Re-*
 1120 *search: Solid Earth*, 97(B2), 1859–1870.
- 1121 Cisternas, M., Atwater, B. F., Torrejón, F., Sawai, Y., Machuca, G., Lagos, M., . . .
 1122 others (2005). Predecessors of the giant 1960 Chile earthquake. *Nature*,
 1123 437(7057), 404.
- 1124 Corbi, F., Funicello, F., Brizzi, S., Lallemand, S., & Rosenau, M. (2017). Control
 1125 of asperities size and spacing on seismic behavior of subduction megathrusts.
 1126 *Geophysical Research Letters*, 44.
- 1127 Crameri, F., Schmeling, H., Golabek, G. J., Duretz, T., Orendt, R., Buitter, S. J. H.,
 1128 . . . Tackley, P. J. (2012). A comparison of numerical surface topography cal-
 1129 culations in geodynamic modelling: an evaluation of the ‘sticky air’ method.
 1130 *Geophysical Journal International*, 189(1), 38–54.
- 1131 Dalguer, L. A., & Day, S. M. (2007). Staggered-grid split-node method for spon-
 1132 taneous rupture simulation. *Journal of Geophysical Research: Solid Earth*,
 1133 112(B2).
- 1134 Dal Zilio, L., van Dinther, Y., Gerya, T. V., & Avouac, J.-P. (2019). Bimodal seis-
 1135 micity in the himalaya controlled by fault friction and geometry. *Nature com-*
 1136 *munications*, 10(1), 48.
- 1137 Dal Zilio, L., van Dinther, Y., Gerya, T. V., & Pranger, C. C. (2018). Seismic be-
 1138 haviour of mountain belts controlled by plate convergence rate. *Earth and*
 1139 *Planetary Science Letters*, 482, 81–92.
- 1140 Das, S. (1980). A numerical method for determination of source time functions for
 1141 general three-dimensional rupture propagation. *Geophysical Journal Interna-*
 1142 *tional*, 62(3), 591–604.
- 1143 Das, S., & Aki, K. (1977a). Fault plane with barriers: a versatile earthquake model.

- 1144 *Journal of geophysical research*, 82(36), 5658–5670.
- 1145 Das, S., & Aki, K. (1977b). A numerical study of two-dimensional spontaneous
1146 rupture propagation. *Geophysical Journal of the Royal Astronomical Society*,
1147 50(3), 643–668.
- 1148 Day, S. M. (1982). Three-dimensional finite difference simulation of fault dynamics:
1149 rectangular faults with fixed rupture velocity. *Bulletin of the Seismological So-*
1150 *ciety of America*, 72(3), 705–727.
- 1151 DeDontney, N., & Hubbard, J. (2012). Applying wedge theory to dynamic rupture
1152 modeling of fault junctions. *Bulletin of the Seismological Society of America*,
1153 102(4), 1693–1711.
- 1154 DeDontney, N., & Rice, J. R. (2012). Tsunami wave analysis and possibility of splay
1155 fault rupture during the 2004 Indian Ocean earthquake. *Pure and applied geo-*
1156 *physics*, 169(10), 1707–1735.
- 1157 DeDontney, N., Rice, J. R., & Dmowska, R. (2012). Finite element modeling of
1158 branched ruptures including off-fault plasticity. *Bulletin of the Seismological*
1159 *Society of America*, 102(2), 541–562.
- 1160 de la Puente, J., Ampuero, J.-P., & Käser, M. (2009). Dynamic rupture modeling on
1161 unstructured meshes using a discontinuous Galerkin method. *Journal of Geo-*
1162 *physical Research: Solid Earth*, 114(B10).
- 1163 Del Gaudio, P., Di Toro, G., Han, R., Hirose, T., Nielsen, S., Shimamoto, T., & Cav-
1164 allo, A. (2009). Frictional melting of peridotite and seismic slip. *Journal of*
1165 *Geophysical Research: Solid Earth*, 114(B6).
- 1166 den Hartog, S. A., Peach, C. J., de Winter, D. M., Spiers, C. J., & Shimamoto, T.
1167 (2012). Frictional properties of megathrust fault gouges at low sliding ve-
1168 locities: New data on effects of normal stress and temperature. *Journal of*
1169 *Structural Geology*, 38, 156–171.
- 1170 Den Hartog, S. A. M., Niemeijer, A. R., & Spiers, C. J. (2012). New constraints
1171 on megathrust slip stability under subduction zone P–T conditions. *Earth and*
1172 *Planetary Science Letters*, 353, 240–252.
- 1173 Dieterich, J. H. (1978). Time-dependent friction and the mechanics of stick-slip. In
1174 *Rock friction and earthquake prediction* (pp. 790–806). Springer.
- 1175 Dieterich, J. H. (1979). Modeling of rock friction: 1. experimental results and consti-
1176 tutive equations. *Journal of Geophysical Research: Solid Earth*, 84(B5), 2161–

- 1177 2168.
- 1178 Di Toro, G., Han, R., Hirose, T., De Paola, N., Nielsen, S., Mizoguchi, K., . . . Shi-
 1179 mamoto, T. (2011). Fault lubrication during earthquakes. *Nature*, *471*(7339),
 1180 494.
- 1181 Drucker, D. C., & Prager, W. (1952). Soil mechanics and plastic analysis or limit de-
 1182 sign. *Quarterly of applied mathematics*, *10*(2), 157–165.
- 1183 Dumbser, M., & Käser, M. (2006). An arbitrary high-order discontinuous Galerkin
 1184 method for elastic waves on unstructured meshes-II. The three-dimensional
 1185 isotropic case. *Geophysical Journal International*, *167*(1), 319–336.
- 1186 Dunham, E. M., & Bhat, H. S. (2008). Attenuation of radiated ground motion
 1187 and stresses from three-dimensional supershear ruptures. *Journal of Geophysi-
 1188 cal Research: Solid Earth*, *113*(B8).
- 1189 Fujiwara, T., Kodaira, S., No, T., Kaiho, Y., Takahashi, N., & Kaneda, Y. (2011).
 1190 The 2011 Tohoku-Oki earthquake: Displacement reaching the trench axis. *Sci-
 1191 ence*, *334*(6060), 1240–1240.
- 1192 Fukao, Y. (1979). Tsunami earthquakes and subduction processes near deep-sea
 1193 trenches. *Journal of Geophysical Research: Solid Earth*, *84*(B5), 2303–2314.
- 1194 Fulton, P., Brodsky, E. E., Kano, Y., Mori, J., Chester, F., Ishikawa, T., . . . oth-
 1195 ers (2013). Low coseismic friction on the Tohoku-Oki fault determined from
 1196 temperature measurements. *Science*, *342*(6163), 1214–1217.
- 1197 Gabriel, A.-A., Ampuero, J.-P., Dalguer, L. A., & Mai, P. M. (2012). The transition
 1198 of dynamic rupture styles in elastic media under velocity-weakening friction.
 1199 *Journal of Geophysical Research: Solid Earth*, *117*(B9).
- 1200 Gabriel, A.-A., Ampuero, J.-P., Dalguer, L. A., & Mai, P. M. (2013, aug). Source
 1201 Properties of Dynamic Rupture Pulses with Off-Fault Plasticity. *Journal of
 1202 Geophysical Research: Solid Earth*, *118*(8), 4117–4126.
- 1203 Gabriel, A.-A., Behrens, J., Bader, M., van Dinther, Y., Gunawan, T., Madden,
 1204 E. H., . . . van Zelst, I. (2018). S21E-0492: Coupled Seismic Cycle - Earth-
 1205 quake Dynamic Rupture - Tsunami Models. In *AGU Fall Meeting 2018*.
 1206 Washington, D.C..
- 1207 Gabriel, A.-A., & Pelties, C. (2014). Simulating Large-Scale Earthquake Dynamic
 1208 Rupture Scenarios On Natural Fault Zones Using the ADER-DG Method.
 1209 In *Geophysical Research Abstracts, EGU General Assembly 2014* (Vol. 16,

- 1210 p. EGU2014-10572).
- 1211 Galis, M., Pelties, C., Kristek, J., Moczo, P., Ampuero, J.-P., & Mai, P. M. (2014).
 1212 On the initiation of sustained slip-weakening ruptures by localized stresses.
 1213 *Geophysical Journal International*, *200*(2), 890–909.
- 1214 Galvez, P., Ampuero, J.-P., Dalguer, L. A., Somala, S. N., & Nissen-Meyer, T.
 1215 (2014). Dynamic earthquake rupture modelled with an unstructured 3-D spec-
 1216 tral element method applied to the 2011 M 9 Tohoku earthquake. *Geophysical*
 1217 *Journal International*, *198*(2), 1222–1240.
- 1218 Galvez, P., Peter, D. B., & Mai, P. M. (2018). Earthquake cycle modeling of curvi-
 1219 linear non-planar faults: 1992, Landers earthquake sequence. In *AGU Fall*
 1220 *Meeting Abstracts*.
- 1221 Gercek, H. (2007). Poisson’s ratio values for rocks. *International Journal of Rock*
 1222 *Mechanics and Mining Sciences*, *44*(1), 1–13.
- 1223 Gerya, T. V. (2010). *Introduction to numerical geodynamic modelling*. Cambridge
 1224 University Press.
- 1225 Gerya, T. V. (2011). Future directions in subduction modeling. *Journal of Geody-*
 1226 *namics*, *52*(5), 344–378.
- 1227 Gerya, T. V., & Meilick, F. (2011). Geodynamic regimes of subduction under an
 1228 active margin: effects of rheological weakening by fluids and melts. *Journal of*
 1229 *Metamorphic Geology*, *29*(1), 7–31.
- 1230 Gerya, T. V., & Yuen, D. A. (2003). Characteristics-based marker-in-cell method
 1231 with conservative finite-differences schemes for modeling geological flows with
 1232 strongly variable transport properties. *Physics of the Earth and Planetary*
 1233 *Interiors*, *140*(4), 293–318.
- 1234 Gerya, T. V., & Yuen, D. A. (2007). Robust characteristics method for modelling
 1235 multiphase visco-elasto-plastic thermo-mechanical problems. *Physics of the*
 1236 *Earth and Planetary Interiors*, *163*(1), 83–105.
- 1237 Goes, S., Agrusta, R., van Hunen, J., & Garel, F. (2017). Subduction-transition zone
 1238 interaction: A review. *Geosphere*, *13*(3), 644–664.
- 1239 Goto, H., Yamamoto, Y., & Kita, S. (2012). Dynamic rupture simulation of the
 1240 2011 off the Pacific coast of Tohoku Earthquake: Multi-event generation within
 1241 dozens of seconds. *Earth, planets and space*, *64*(12), 11.
- 1242 Hardebeck, J. L. (2012). Coseismic and postseismic stress rotations due to great

- 1243 subduction zone earthquakes. *Geophysical Research Letters*, *39*(21).
- 1244 Hardebeck, J. L. (2015). Stress orientations in subduction zones and the strength of
1245 subduction megathrust faults. *Science*, *349*(6253), 1213–1216.
- 1246 Harris, R. A. (2004). Numerical simulations of large earthquakes: Dynamic rupture
1247 propagation on heterogeneous faults. In A. Donnellan, P. Mora, M. Matsu'ura,
1248 & X.-C. Yin (Eds.), *Computational earthquake science part ii* (pp. 2171–2181).
1249 Basel: Birkhäuser Basel. doi: 10.1007/978-3-0348-7875-3_5
- 1250 Harris, R. A., Barall, M., Aagaard, B., Ma, S., Roten, D., Olsen, K., . . . Dalguer, L.
1251 (2018). A suite of exercises for verifying dynamic earthquake rupture codes.
1252 *Seismological Research Letters*, *89*(3), 1146.
- 1253 Harris, R. A., Barall, M., Andrews, D., Duan, B., Ma, S., Dunham, E., . . . others
1254 (2011). Verifying a computational method for predicting extreme ground
1255 motion. *Seismological Research Letters*, *82*(5), 638–644.
- 1256 Harris, R. A., Barall, M., Archuleta, R., Dunham, E., Aagaard, B., Ampuero, J., . . .
1257 others (2009). The SCEC/USGS dynamic earthquake rupture code verification
1258 exercise. *Seismological Research Letters*, *80*(1), 119–126.
- 1259 Heinecke, A., Breuer, A., Rettenberger, S., Bader, M., Gabriel, A.-A., Pelties, C., . . .
1260 others (2014). Petascale high order dynamic rupture earthquake simulations on
1261 heterogeneous supercomputers. In *SC14: Proceedings of the International Con-*
1262 *ference for High Performance Computing, Networking, Storage and Analysis*
1263 (pp. 3–14).
- 1264 Herrendörfer, R. (2018). *Modeling of the slip spectrum along mature and spon-*
1265 *taneously forming faults in a visco-elasto-plastic continuum* (Unpublished
1266 doctoral dissertation). ETH Zurich.
- 1267 Herrendörfer, R., Gerya, T. V., & van Dinther, Y. (2018). An invariant rate-and
1268 state-dependent friction formulation for visco-elasto-plastic earthquake cycle
1269 simulations. *Journal of Geophysical Research: Solid Earth*.
- 1270 Herrendörfer, R., Van Dinther, Y., Gerya, T. V., & Dalguer, L. A. (2015). Earth-
1271 quake supercycle in subduction zones controlled by the width of the seismo-
1272 genic zone. *Nature Geoscience*, *8*(6), 471.
- 1273 Huang, Y., Ampuero, J.-P., & Helmberger, D. V. (2014). Earthquake ruptures
1274 modulated by waves in damaged fault zones. *Journal of Geophysical Research:*
1275 *Solid Earth*, *119*(4), 3133–3154.

- 1276 Huang, Y., Meng, L., & Ampuero, J.-P. (2013). A dynamic model of the frequency-
1277 dependent rupture process of the 2011 Tohoku-Oki earthquake. *Earth, planets*
1278 *and space*, *64*(12), 1.
- 1279 Ida, Y. (1973). The maximum acceleration of seismic ground motion. *Bulletin of the*
1280 *Seismological Society of America*, *63*(3), 959–968.
- 1281 Kame, N., Rice, J. R., & Dmowska, R. (2003). Effects of prestress state and rupture
1282 velocity on dynamic fault branching. *Journal of Geophysical Research: Solid*
1283 *Earth*, *108*(B5).
- 1284 Kaneko, Y., Ampuero, J.-P., & Lapusta, N. (2011). Spectral-element simulations of
1285 long-term fault slip: Effect of low-rigidity layers on earthquake-cycle dynamics.
1286 *Journal of Geophysical Research: Solid Earth*, *116*(B10).
- 1287 Kaus, B. J. (2010). Factors that control the angle of shear bands in geodynamic nu-
1288 merical models of brittle deformation. *Tectonophysics*, *484*(1-4), 36–47.
- 1289 Kodaira, S., Kurashimo, E., Park, J.-O., Takahashi, N., Nakanishi, A., Miura, S.,
1290 ... Kaneda, Y. (2002). Structural factors controlling the rupture process of
1291 a megathrust earthquake at the Nankai trough seismogenic zone. *Geophysical*
1292 *Journal International*, *149*(3), 815–835.
- 1293 Kopf, A., & Brown, K. M. (2003). Friction experiments on saturated sediments and
1294 their implications for the stress state of the Nankai and Barbados subduction
1295 thrusts. *Marine Geology*, *202*(3-4), 193–210.
- 1296 Kostrov, B. V. (1964). Self similar problems of propagation of shear cracks. *Journal*
1297 *of Applied Mathematics and Mechanics*, *28*(5), 1077–1087.
- 1298 Kozdon, J. E., & Dunham, E. M. (2013). Rupture to the trench: Dynamic rupture
1299 simulations of the 11 March 2011 Tohoku earthquake. *Bulletin of the Seismo-*
1300 *logical Society of America*, *103*(2B), 1275–1289.
- 1301 Kozdon, J. E., Dunham, E. M., & Nordström, J. (2013). Simulation of dynamic
1302 earthquake ruptures in complex geometries using high-order finite difference
1303 methods. *Journal of Scientific Computing*, *55*(1), 92–124.
- 1304 Lallemand, S., Heuret, A., & Boutelier, D. (2005). On the relationships between
1305 slab dip, back-arc stress, upper plate absolute motion, and crustal nature in
1306 subduction zones. *Geochemistry, Geophysics, Geosystems*, *6*(9).
- 1307 Langer, S., Olsen-Kettle, L. M., Weatherley, D., Gross, L., & Mühlhaus, H.-B.
1308 (2010). Numerical studies of quasi-static tectonic loading and dynamic rup-

- 1309 ture of bi-material interfaces. *Concurrency and Computation: Practice and*
1310 *Experience*, 22(12), 1684–1702.
- 1311 Lapusta, N., Rice, J. R., Ben-Zion, Y., & Zheng, G. (2000). Elastodynamic analysis
1312 for slow tectonic loading with spontaneous rupture episodes on faults with
1313 rate-and state-dependent friction. *Journal of Geophysical Research: Solid*
1314 *Earth*, 105(B10), 23765–23789.
- 1315 Lay, T., Ammon, C. J., Kanamori, H., Xue, L., & Kim, M. J. (2011). Possible
1316 large near-trench slip during the 2011 Mw 9.0 off the Pacific coast of Tohoku
1317 Earthquake. *Earth, planets and space*, 63(7), 32.
- 1318 Li, S., Moreno, M., Rosenau, M., Melnick, D., & Oncken, O. (2014). Splay fault
1319 triggering by great subduction earthquakes inferred from finite element models.
1320 *Geophysical Research Letters*, 41(2), 385–391.
- 1321 Liu, Y., & Rice, J. R. (2007). Spontaneous and triggered aseismic deformation
1322 transients in a subduction fault model. *Journal of Geophysical Research: Solid*
1323 *Earth*, 112(B9).
- 1324 Lotto, G. C., Dunham, E. M., Jeppson, T. N., & Tobin, H. J. (2017). The effect
1325 of compliant prisms on subduction zone earthquakes and tsunamis. *Earth and*
1326 *Planetary Science Letters*, 458, 213–222.
- 1327 Ma, S. (2012). A self-consistent mechanism for slow dynamic deformation and
1328 tsunami generation for earthquakes in the shallow subduction zone. *Geophysi-*
1329 *cal Research Letters*, 39(11).
- 1330 Madariaga, R., Olsen, K., & Archuleta, R. (1998). Modeling dynamic rupture in
1331 a 3D earthquake fault model. *Bulletin of the Seismological Society of America*,
1332 88(5), 1182–1197.
- 1333 Madden, E. H., Ulrich, T., Gabriel, A.-A., van Zelst, I., & van Dinther, Y. (2017).
1334 The role of splay faults in seafloor deformation and tsunami generation dur-
1335 ing the Mw 9.1-9.3 Sumatra-Andaman Earthquake. In E. E. Gdoutos (Ed.),
1336 *Proceedings of the 14th international conference on fracture*.
- 1337 Madden, E. H., Ulrich, T., Rannabauer, L., Vater, S., Gabriel, A.-A., Behrens, J.,
1338 ... van Zelst, I. (2018). Physics-based Coupled Models of the 2018 Sulawesi
1339 Earthquake and Tsunami. In *AGU Fall Meeting Abstracts*.
- 1340 Murphy, S., Scala, A., Herrero, A., Lorito, S., Festa, G., Trasatti, E., ... Nielsen, S.
1341 (2016). Shallow slip amplification and enhanced tsunami hazard unravelled by

- 1342 dynamic simulations of mega-thrust earthquakes. *Scientific reports*, 6, 35007.
- 1343 Nielsen, S., & Madariaga, R. (2003). On the self-healing fracture mode. *Bulletin of*
 1344 *the Seismological Society of America*, 93(6), 2375–2388.
- 1345 Oeser, J., Bunge, H.-P., & Mohr, M. (2006). Cluster design in the earth sciences:
 1346 Tethys. In *International conference on high performance computing and com-*
 1347 *munications* (pp. 31–40).
- 1348 Oglesby, D. D., Archuleta, R. J., & Nielsen, S. B. (1998). Earthquakes on dipping
 1349 faults: the effects of broken symmetry. *Science*, 280(5366), 1055–1059.
- 1350 Olsen-Kettle, L., Weatherley, D., Saez, E., Gross, L., Mühlhaus, H.-B., & Xing, H.
 1351 (2008). Analysis of slip-weakening frictional laws with static restrengthen-
 1352 ing and their implications on the scaling, asymmetry, and mode of dynamic
 1353 rupture on homogeneous and bimaterial interfaces. *Journal of Geophysical*
 1354 *Research: Solid Earth*, 113(B8).
- 1355 Patočka, V., Čadek, O., Tackley, P. J., & Čížková, H. (2017). Stress memory ef-
 1356 fect in viscoelastic stagnant lid convection. *Geophysical Journal International*,
 1357 209(3), 1462–1475.
- 1358 Pelties, C., Gabriel, A.-A., & Ampuero, J.-P. (2014). Verification of an ADER-DG
 1359 method for complex dynamic rupture problems. *Geoscientific Model Develop-*
 1360 *ment*, 7(3), 847–866.
- 1361 Pelties, C., Huang, Y., & Ampuero, J.-P. (2015). Pulse-like rupture induced by
 1362 three-dimensional fault zone flower structures. *Pure and Applied Geophysics*,
 1363 172(5), 1229–1241.
- 1364 Pelties, C., Puente, J., Ampuero, J.-P., Brietzke, G. B., & Käser, M. (2012). Three-
 1365 dimensional dynamic rupture simulation with a high-order discontinuous
 1366 Galerkin method on unstructured tetrahedral meshes. *Journal of Geophysical*
 1367 *Research: Solid Earth*, 117(B2).
- 1368 Petrini, C., Gerya, T. V., van Dinther, Y., Connolly, J. A., & Madonna, C. (2017).
 1369 Modelling earthquakes using a poro-elastic two-phase flow formulation. In
 1370 *AGU Fall Meeting Abstracts*.
- 1371 Preiswerk, L., van Dinther, Y., & Gerya, T. V. (in press). A secondary zone of uplift
 1372 caused by megathrust earthquakes. *Pure and Applied Geophysics*.
- 1373 Preuss, S., Herrendrfer, R., Gerya, T. V., Ampuero, J.-P., & van Dinther, Y. (2019,
 1374 Jan). *Seismic and aseismic fault growth lead to different fault orientations*.

- 1375 EarthArXiv.
- 1376 Ranalli, G. (1995). *Rheology of the earth*. Springer Science & Business Media.
- 1377 Rice, J. R. (1993). Spatio-temporal complexity of slip on a fault. *Journal of Geo-*
 1378 *physical Research: Solid Earth*, 98(B6), 9885–9907.
- 1379 Romanet, P., Bhat, H. S., Jolivet, R., & Madariaga, R. (2018). Fast and slow slip
 1380 events emerge due to fault geometrical complexity. *Geophysical Research Let-*
 1381 *ters*, 45(10), 4809–4819.
- 1382 Ruina, A. (1983). Slip instability and state variable friction laws. *Journal of Geo-*
 1383 *physical Research: Solid Earth*, 88(B12), 10359–10370.
- 1384 Schultz, R. (1995). Limits on strength and deformation properties of jointed basaltic
 1385 rock masses. *Rock Mechanics and Rock Engineering*, 28(1), 1–15.
- 1386 Seno, T. (2009). Determination of the pore fluid pressure ratio at seismogenic
 1387 megathrusts in subduction zones: Implications for strength of asperities and
 1388 Andean-type mountain building. *Journal of Geophysical Research: Solid Earth*,
 1389 114(B5).
- 1390 Sobolev, S. V., & Muldashev, I. A. (2017). Modeling seismic cycles of great megath-
 1391 rust earthquakes across the scales with focus at postseismic phase. *Geochem-*
 1392 *istry, Geophysics, Geosystems*, 18(12), 4387–4408.
- 1393 Stein, S., & Wysession, M. (2009). *An introduction to seismology, earthquakes, and*
 1394 *earth structure*. John Wiley & Sons.
- 1395 Tamura, S., & Ide, S. (2011). Numerical study of splay faults in subduction zones:
 1396 The effects of bimaterial interface and free surface. *Journal of Geophysical Re-*
 1397 *search: Solid Earth*, 116(B10).
- 1398 Tsutsumi, A., & Shimamoto, T. (1997). High-velocity frictional properties of gabbro.
 1399 *Geophysical Research Letters*, 24(6), 699–702.
- 1400 Turcotte, D., & Schubert, G. (2002). *Geodynamics*. Cambridge University Press.
- 1401 Ujiie, K., Tanaka, H., Saito, T., Tsutsumi, A., Mori, J. J., Kameda, J., ... Scien-
 1402 tists, T. (2013). Low Coseismic Shear Stress on the Tohoku-Oki Megathrust
 1403 Determined from Laboratory Experiments. *Science*, 342(6163), 1211–1214.
 1404 doi: 10.1126/science.1243485
- 1405 Ulrich, T., Gabriel, A.-A., Ampuero, J.-P., & Xu, W. (2018, Jul). *Dynamic viability*
 1406 *of the 2016 Mw 7.8 Kaikura earthquake cascade on weak crustal faults*. Earth-
 1407 ArXiv.

- 1408 Uphoff, C., Rettenberger, S., Bader, M., Madden, E. H., Ulrich, T., Wollherr, S., &
 1409 Gabriel, A.-A. (2017). Extreme scale multi-physics simulations of the tsunami-
 1410 genic 2004 sumatra megathrust earthquake. In *Proceedings of the international*
 1411 *conference for high performance computing, networking, storage and analysis*
 1412 (p. 21).
- 1413 van Dinther, Y., Gerya, T. V., Dalguer, L. A., Corbi, F., Funiciello, F., & Mai,
 1414 P. M. (2013). The seismic cycle at subduction thrusts: 2. Dynamic implica-
 1415 tions of geodynamic simulations validated with laboratory models. *Journal of*
 1416 *Geophysical Research: Solid Earth*, *118*(4), 1502–1525.
- 1417 van Dinther, Y., Gerya, T. V., Dalguer, L. A., Mai, P. M., Morra, G., & Giardini,
 1418 D. (2013). The seismic cycle at subduction thrusts: Insights from seismo-
 1419 thermo-mechanical models. *Journal of Geophysical Research: Solid Earth*,
 1420 *118*(12), 6183–6202.
- 1421 van Dinther, Y., Mai, P. M., Dalguer, L. A., & Gerya, T. V. (2014). Modeling the
 1422 seismic cycle in subduction zones: The role and spatiotemporal occurrence of
 1423 off-megathrust earthquakes. *Geophysical Research Letters*, *41*(4), 1194–1201.
- 1424 Wang, K., & Hu, Y. (2006). Accretionary prisms in subduction earthquake cy-
 1425 cles: The theory of dynamic Coulomb wedge. *Journal of Geophysical Research:*
 1426 *Solid Earth*, *111*(B6).
- 1427 Wendt, J., Oglesby, D. D., & Geist, E. L. (2009). Tsunamis and splay fault dynam-
 1428 ics. *Geophysical Research Letters*, *36*(15).
- 1429 Wollherr, S., Gabriel, A.-A., & Mai, P. M. (2018). *Landers 1992 "reloaded": an inte-*
 1430 *grative dynamic earthquake rupture model*. EarthArXiv.
- 1431 Wollherr, S., Gabriel, A.-A., & Uphoff, C. (2018). Off-fault plasticity in three-
 1432 dimensional dynamic rupture simulations using a modal Discontinuous
 1433 Galerkin method on unstructured meshes: Implementation, verification,
 1434 and application. *Geophysical Journal International*, *214*, 1556–1584. doi:
 1435 <https://doi.org/10.1093/gji/ggy213>
- 1436 Wollherr, S., van Zelst, I., Gabriel, A.-A., van Dinther, Y., Madden, E. H., & Ulrich,
 1437 T. (2017). Dynamic rupture models of subduction zone earthquakes with
 1438 off-fault plasticity. In *AGU Fall Meeting Abstracts*.